Russian Chemical Reviews **72** (2) 165 – 191 (2003) © 2003 Russian Academy of Sciences and Turpion Ltd

DOI 10.1070/RC2003v072n02ABEH000744

Non-traditional applications of NMR tomography

I V Koptyug, R Z Sagdeev

Contents

I.	Introduction	165
II.	Chemical reactions	165
III.	Magnetic resonance thermometry	169
IV.	Magnetic resonance current density imaging	172
V.	NMR imaging of gases	173
VI.	Magnetic resonance imaging of solids	177
VII.	Supplement	180

Abstract. Applications of NMR imaging to studies of chemical reactions including polymerisation reactions and the Belousov–Zhabotinsky oscillating reaction are considered. Publications concerning applications of NMR imaging to studies of the temperature and electric current density distributions in various specimens are discussed. NMR investigations of hyperpolarised gases and gases with equilibrium nuclear spin polarisation are described. NMR imaging studies of solids (in particular, polymers and elastomers) are briefly outlined. The bibliography includes 275 references.

I. Introduction

Investigations of chemical reactions *in situ* is a promising field of application of NMR tomography (or magnetic-resonance imaging, MRI). Currently, this field has attracted considerable attention of researchers. In this review we present a detailed consideration of the studies concerned with applications of NMR imaging to the determination of the temperature and electric current density distributions within various objects. Most of these studies were carried out to address biomedical problems; however, experimental MRI techniques can undoubtedly be useful for physicochemical investigations and chemical technology. A large section of this review concerns MRI of gases. A vast area of MRI studies of solid materials is only briefly outlined owing to specific features of solid-state NMR spectroscopy. However, some solid materials, such as polymers and elastomers, allow liquid-phase NMR techniques to be employed. In this connection mention may be made that applications of NMR imaging to studies of liquid-containing materials and mass transfer investigations have been the subject of our recent reviews.[1,2]

I V Koptyug, R Z Sagdeev International Tomography Centre, Siberian Branch of the Russian Academy of Sciences, ul. Institutskaya 3A, 630090 Novosibirsk, Russian Federation. Fax (7-383) 233 13 99. Tel. (7-383) 233 35 61. E-mail: koptyug@tomo.nsc.ru (I V Koptyug). Tel. (7-383) 233 14 48. E-mail: itc@tomo.nsc.ru (R Z Sagdeev)

Received 20 June 2002
Uspekhi Khimii **72** (2) 183 – 212 (2003); translated by A M Raevsky

II. Chemical reactions

1. General remarks

Currently, NMR spectroscopy is widely used in studies of chemical reactions. However, there are only a few reports on the use of NMR imaging for these purposes despite a steady interest in this kind of experimental research.

Currently, there are only two fields of application that have attracted considerable attention of researchers. One of them is the application of NMR microimaging, or magnetic resonance microimaging (MRM), to studies of polymerisation processes. Polymerisation is often accompanied by slowing down the molecular mobility, which can lead to substantial reduction of the spin – spin relaxation times (T_2) of the nuclei under study. This allows one to selectively follow variations of the spatial distribution of the initial reagents with time. Usually, polymers are characterised by short T_2 times and, hence, NMR signals of these substances are not often observed. The polymer matrix reduces the mobility of the residual monomer, and the T_2 time of the latter shortens as well. To enhance the NMR signal of the polymer, one can use the fact that an increase in temperature accelerates the molecular mobility. In the case of gel formation the system can be imaged using the signal of the more mobile, liquid dispersion medium. Yet another approach involves introduction of various tracers into the initial mixture. Tracers are not involved in the reaction, but reflect variations of the local viscosity of the medium during polymerisation.

Another field of successful application of the MRM technique is the study of the Belousov–Zhabotinsky (B–Z) oscillating reactions, *i.e.*, metal ion-catalysed oxidation of organic compounds by bromate ions.[3] In this case the water proton chemical shifts and relaxation times are linear functions of the concentration of the paramagnetic metal ion present in the aqueous solution and are affected by the oxidised and reduced states of the metal ion in a different manner.

Some other reactions have also been studied using MRI techniques. Of particular importance is the possibility of determining the local chemical composition of the reaction mixture by recording spatially resolved NMR spectra and selective NMR imaging using a particular NMR signal.

2. Thermal polymerisation

The formation of poly(methyl methacrylate) (PMMA) was monitored[4] by the disappearance of the signal of methyl methacrylate (MMA) mixed with the initiator in a mould pre-heated to 60 °C.

The two-dimensional (2D) NMR images obtained revealed mainly homogeneous propagation of the polymerisation process from the centre of the sample towards its periphery. However, the images clearly exhibit a small 'defect', namely, a region in which the polymerisation proceeds at a lower rate. The presence of this defect was confirmed visually.[4] Homogeneous polymerisation of MMA was also reported by other authors (see, *e.g.*, Ref. 5). Polymerisation in the course of the formation of an aqueous gel of cross-linked poly(methacrylic acid) was investigated by recording T_2-weighted 2D images.[6] An increase in the sample viscosity with time was found to shorten the T_2 time of the sample.

Copolymerisation of methacrylamide with *N*,*N*′-methylenebisacrylamide in water has also been studied.[7] The process began upon the addition of ammonium persulfate (initiator) and tetramethylethylenediamine (accelerator). Polymerisation reduces the T_1 time of the signals observed. Two-dimensional NMR images obtained using the NMR signal of water revealed homogeneous gel formation throughout the sample (no polymerisation front was observed).[7]

When preparing epoxy resin based composites, it is of great importance to have a means for monitoring variations of the state of the composite during the cross-linking of polymer chains at elevated temperature.[8,9] Raising the temperature causes an increase in the T_2 time of the resin; therefore, at temperatures above 55 °C one can obtain NMR images during the cross-linking of resin reinforced with carbon fibres using the signal from the resin protons.[8] At times of the order of 5 min after heating to 100 °C, the cross-linking degree of the polymer chains is low and the viscosity of the sample is a function of the temperature only. Therefore, the use of corresponding calibration allows the viscosity or temperature distribution to be mapped throughout the sample. Analysis of a set of NMR images acquired at 90 °C revealed that the cross-linking at the periphery of the sample proceeds at a higher rate.

To prepare a composite material, layers of aligned carbon fibres soaked with partially cured polymer were stacked in such a manner that the fibres in each layer have different orientation.[4] The stack obtained was placed in a mould and hot vulcanised. Before vulcanisation the polymer exhibited a short time T_2 which increased during the heat treatment procedure due to an increase in the polymer mobility. As a result, an NMR signal appeared in the corresponding regions of the 2D NMR image. Further vulcanisation led to a decrease in T_2 and to disappearance of the NMR signal. Such a signal variation in the case of unilateral heating allows one to observe how the vulcanisation process propagates throughout the sample as a single wave.[4] Rubber vulcanisation has also been studied.[10,11]

If a chemical reaction is coupled to molecular diffusion, a reaction front moving at a constant velocity can appear in the system. Autocatalytic polymerisation of methacrylic acid [12] is due to the exothermic character of free-radical polymerisation and to thermal decomposition of the initiator (benzoyl peroxide), which is accompanied by generation of free radicals. Polymerisation causes a substantial shortening of the T_2 time for both the polymer and the solvent. The reaction was initiated by adding accelerator (*N*,*N*-dimethylaniline) on the surface of the methacrylic acid–benzoyl peroxide mixture. Then, an induction period was observed, where the reaction front moved downward slowly with variable velocity. The duration of the induction period (4–14 min) appeared to be related to the mixing degree of the reagents in the surface layer upon addition of the accelerator. After the induction period the reaction suddenly accelerated, but rapid movement of the reaction front settled into a constant velocity of ~ 0.6 cm min^{-1}. NMR imaging studies using the ^{1}H NMR signal of the monomer (and aniline) and companion experiments using the ^{19}F nuclei of 1,4-dibromotetrafluorobenzene (tracer) led to similar results. The front length exceeded 1 mm while its shape remained unchanged with time. An NMR signal with good signal-to-noise ratio was observed in the region immediately behind the reaction front. This indicated the presence of the residual monomer after passage of the reaction front. The experiments were carried out at room temperature; the temperature near the reaction front increased to 176 °C. Attempts at detecting the effect of the magnetic field on the reaction rate failed.[12]

3. Photoinduced and radiation induced polymerisation

Various types of radiation induced polymerisation are widely used in technological processes. Fabrication of various polymeric coatings, use of photosensitive dental materials for stomatology, creation of relief images in lithography can serve as examples of practical implementation of photoinduced polymerisation. Flexible photopolymer printing boards comprise layers of a rubber-like polymer, bifunctional monomer, photoinitiator, dyes and stabilisers. The unexposed regions of the plate are usually removed by solvent. In this case NMR imaging can be used for visualisation of the irradiated region before developing the board.[4]

Photoinduced polymerisation of a resin containing methacrylic monomers has been studied (the process was induced by irradiation with visible light at 470 nm).[13] This material is used in stomatology. Shrinkage of the material due to polymerisation can be as high as 10%, thus shortening its lifetime and deteriorating properties. The polymerisation kinetics of the resin was studied by spatially resolved NMR imaging techniques. It was found that the polymerisation rate increases with the distance from the irradiated free surface of the sample due to the inhibiting action of dioxygen. As a result, after irradiation the surface layer of the sample (layer thickness 500 μm) was found to contain a large amount of the monomer.

Photoinduced polymerisation of hexamethylene dimethylacrylate using various concentrations of benzyl-dimethyl ketal as photoinitiator has been studied [14] by means of chemical shift selective NMR imaging techniques with different monomer proton groups. As the content of the initiator was 1.5%, the degree of conversion was 20% and a gel-like state was formed; the T_2 times for different proton groups varied in a different manner. Lengthening the exposure time led to a sharper boundary between the polymer and the rest of the sample. An NMR imaging study of photoinduced polymerisation of 1,6-hexanediol dimethacrylate using the same initiator has been reported.[15] In this case NMR images were acquired at different exposure times. Polymerisation began at the centre of the ampoule because of light focussing at the bottom. The polymerisation front was ~ 50 μm long. The residual monomer was observed in the near-wall region. In some instances a rather thick monomer layer (due to oxygen diffusion) was observed adjacent to the free surface through which it was irradiated.[14,15]

Radiation-induced polymerisation can be used for dosimetry in the case of irradiation with X- or γ-rays, proton beams, *etc*. An important application of MRI is the determination of the spatial distribution of the absorbed dose when using stereotaxic irradiation in radiation therapy of various diseases. Modern experimental methods allow high irradiation doses to be delivered to a small volume of a complex shape. The MRM technique [1] permits spatial (3D) visualisation of the irradiated zones using various gel-based dosimeters.[16] Applications of gels containing the Fricke dosimetric solution is based on the radiation-induced transformation of Fe(II) into Fe(III), which causes reduction of the spin–lattice relaxation time, T_1, of the solvent (ferrous-based MRI dosimetry, or FeMRI). The amount of newly formed Fe(III) is a linear function of the irradiation dose. The 'null-point' technique, which allows one to follow the movement of the region with the prescribed concentration of the paramagnetic tracer, was used to study the diffusion of Fe^{2+} and Fe^{3+} ions in agarose gel.[17] Due to fast diffusion displacements of the ions the irradiation dose distribution over the sample should be studied within several hours after the irradiation. The sensitivity of the FeMRI technique to irradiation is low. NMR images of the X-ray or proton beam irradiated samples have been obtained and an improved T_1 mapping procedure has been reported.[18]

MRI applications of polymer gels, whose properties are similar to those of tissues in living organisms, are based on irradiation-induced polymerisation of a monomer dispersed in the gel (the so-called 'Polymerisation Based Dosimeter Gel Evaluated Using MRI' procedure, or PoMRI). This kind of dosimeter can be based on, *e.g.*, an aqueous gelatin gel with the addition of acrylic comonomers and cross-linking agents. Irradiation causes the generation of free radicals that initiate both polymerisation and cross-linking of the monomer molecules.[19,20] Analysis of the T_2 maps obtained for irradiated polyacrylamide gels showed that polymerisation is not complete even several weeks after irradiation. Oxygen inhibits polymerisation; however, this was observed only in the near-surface layer due to slow oxygen diffusion. For thoroughly prepared samples the relaxation rates $1/T_1$ and $1/T_2$ appeared to be linear functions of the irradiation dose in the range from 0 to 10 Gy.[20] In the non-irradiated gels the T_2 value also decreased with time, which seems to be due to the presence of impurities in freshly prepared samples (radicals capable of initiating polymerisation).[19] For *N*,*N*′-bisacrylamide gels the relaxation rate $1/T_2$ is a linear function of the irradiation dose up to saturation levels of 10 to 15 Gy.[16,21] The T_2 maps obtained for these gels were converted into the spatial irradiation dose maps using the formula

$$\frac{1}{T_2} = 6.0 + 0.48\,D,$$

where D is the irradiation dose (in Gy).[16] *N*-Vinylpyrrolidone-based gels (VIPAR) exhibit lower toxicity; however, they are less sensitive to radiation.[21]

$$\frac{1}{T_2} = \frac{1}{T_{20}} + 0.09\,D,$$

where T_{20} is the T_2 time of the gel before irradiation. A linear response was observed up to 32 Gy doses. The spatial distribution of the irradiation dose in these gels has also been studied.

4. The Belousov – Zhabotinsky reaction

A number of publications have been concerned with the NMR imaging studies of 'chemical' (concentration) oscillations and waves observed in the manganese-catalysed oxidation of malonic acid by bromate ion (Fig. 1). The system under study is optically transparent, which makes visual monitoring of various processes difficult. However, there is a linear correlation between the water proton chemical shift and relaxation times and the concentration of the paramagnetic metal ion in the aqueous solution. The reduced state of the manganese ion (Mn^{2+}) is known to affect these parameters more than the oxidised state (Mn^{3+}).[22] The spin – spin relaxation time is most sensitive to the change in the oxidation state of manganese. Therefore, usually T_2-weighted NMR images are used, in which the regions with higher concentrations of Mn^{3+} ions (reaction front or oxidation stage) give a stronger NMR signal compared to the regions with lower concentrations of Mn^{3+} ions. Instability of manganese in the 3+ state in aqueous solutions can lead to a loss of image contrast; therefore, the reaction mixture is doped with orthophosphoric acid ($\sim$1 mol litre^{-1}) to stabilise the Mn^{3+} ion due to the formation of the metal – phosphate complex.[22] The formation of more stable chelate complexes in the case of polydentate phosphate ligands causes a substantial increase in the T_2 time of the water protons in the oxidation stage even when much smaller amounts of dopants ($Na_4P_2O_7$ or $Na_5P_3O_{10}$) are used. This offers some advantages.[23] At the same time, the water proton relaxation time T_1 also increases, thus leading to a loss of image contrast or to image inversion.[23] In addition, variation of stability of the metal – ligand complex can cause changes in the period of the concentration oscillations.[23] To prevent gas liberation (*via* bubbling), the experiments are often carried out in tightly closed containers.

When studying the behaviour of trigger waves in the excitable (non-oscillating) B – Z system, agar is added to the solution to form gels and to suppress undesired convective flows in the medium due to an increase in the medium viscosity. 2D NMR images of the spiral waves in pseudo-2D thin gel layers and the 2D cross-sections of spherical waves in a cylindrical ampoule acquired at different instants have been reported.[24] This allowed visualisation of wave propagation and collisional annihilation. The advantage of the NMR imaging technique is the possibility of obtaining 3D images of the wave front. In combination with the achievements of modern computer graphics this makes it possible to construct 3D images of complex waves (*e.g.*, a twisted scroll wave) and thus investigate the evolution of the organising filamentary singularities of the wave concentration structures.[25]

A simple procedure for fast imaging of the wave front propagation has been proposed by Tzalmona *et al.*[26] taking cerium-catalysed oxidation of citric acid by potassium bromate as an example. The technique involves 1D slice selective NMR imaging with slice projection on an axis in the slice plane. One-dimensional NMR images are successively acquired at a constant time delay (Fig. 2). By stacking the 1D NMR images one can obtain a 2D image in the displacement – time coordinates, where the regions of highly intense signals form inclined bands, their slopes being a measure of the wave front propagation velocity. If a concentration wave propagates at a constant velocity, the bands look like slant lines. Menzinger *et al.*[27] studied chemical waves in the Belousov – Zhabotinsky reaction in a non-viscous solution containing no agar. They found that the ascending portion of the spherically expanding wave becomes unstable and drastically accelerates, being developed in a plume-like cloud. At the same time, the descending portion of the wave travels unperturbed and at a constant velocity. The reason for instability of the ascending wave is an isothermal decrease in the medium density in the region after the oxidation front, resulting in the appearance of convective flows. Simultaneously, subsidiary pacemakers appear in the instability region, emitting new waves.[27] The 1D projection



Figure 1. Travelling concentration waves in the oxidation of malonic acid in an ampoule 5 mm in diameter filled with glass beads 0.5 mm in diameter.
A spherical wave is created in the bottom region of the sample (see the right side of the NMR image) and then partially annihilated upon collision with the ampoule wall. The remaining part of the wave front continues to propagate through the medium (see the left side of the NMR image). The 2D NMR image was obtained using the axial slice selection technique.

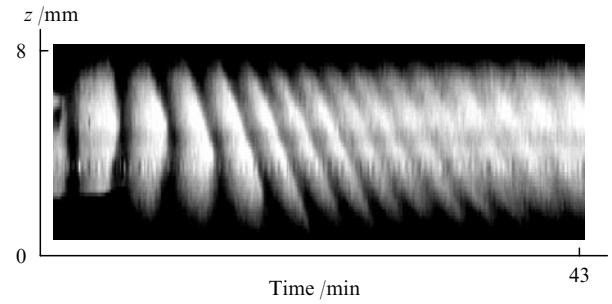


Figure 2. Concentration oscillations and concentration waves in the oxidation of citric acid.
Bright bands correspond to higher concentrations of Ce(III) and dark bands correspond to the oxidised state, Ce(IV). The reaction was conducted in water doped with starch (1%); the 1D projections of the reaction mixture on the axis of an ampoule 5 mm in diameter were obtained without slice selection.

technique was also employed to determine the activation energies for wave front propagation and wave emission by the pacemaker [28] and to obtain a dispersion curve that illustrates the interrelation between the wave propagation velocity and the pacemaker activity period.[29]

Chemical waves in the B–Z system can also be used as an indicator of the fluid motion in the imaging of, *e.g.*, temperature-gradient driven convective flows. NMR imaging experiments using the 1D projection technique (see above) revealed wave-front distortions due to convection in a cylindrical sample which was heated and then allowed to gradually cool inside the probe of the NMR spectrometer.[28] An increase in the temperature gradient (Rayleigh number) due to the heating of the sample to higher temperatures led to the onset of the principal and then the lowest excited critical convection modes.

NMR imaging was also used for studying the self-oscillatory B–Z system in which not only trigger, but also phase waves are observed. The latter are not accompanied by mass transfer and represent a purely optical effect, which is due to the phase or frequency difference between the oscillations at different points of space. Kinematic waves (a kind of phase wave) originate from the temperature difference between different points of the sample. The 1D wave projection technique has been successfully employed in the investigations of the wave dynamics in the self-oscillatory B–Z system. Here, kinematic waves arose from frequency gradients in an anisotropically cooling sample.[30]

An increase in the oscillation phase gradients is always accompanied by an increase in the concentration gradients in the sample. This gradually makes the role of diffusion increasingly important. As a result, conversion occurs of kinematic waves into diffusion-driven ones and the wave propagation velocity no longer decreases, thus reaching a limiting value corresponding to the velocity of chemical waves. A study of the interaction between trigger waves and kinematic waves showed that wave collision patterns can be incorrectly interpreted as a sudden acceleration of trigger waves.[26]

Armstrong *et al.*[31] reported an NMR imaging study of kinematic waves in the B–Z reaction catalysed by various metal ions. The technique requires that the effects of the oxidised and reduced states of the catalyst on the NMR parameters of water protons be different. In the case of cerium-catalysed oxidation of malonic acid the proton relaxation times of water in the presence of Ce(III) and Ce(IV) differ insignificantly, so only the 1D projections of the wave front were recorded. When ruthenium ($[Ru(bipy)_3]^{2+}$, where bipy is bipyridyl) was used to catalyse the same reaction, the relaxation times of water varied over a somewhat wider range compared to the Ce-catalysed reaction and 2D NMR images of waves were also obtained. It should be noted that, in contrast to manganese and cerium, shorter relaxation times for the Ru-catalysed reaction were obtained for the oxidised state, Ru(III), rather than the reduced state, Ru(II). Therefore, the best contrast for the reaction with ruthenium should be expected for T_1-weighted images. Attempts at NMR imaging a ferroin-catalysed B–Z reaction (ferroin is $[(Fe(phen)_3]^{2+}$, where phen is phenanthroline) failed despite considerably different effects of ferroin and ferriin ($[Fe(phen)_3]^{3+}$) on the T_2 time of water. Armstrong *et al.* [31] suggested that in this case the relaxation times are mainly affected by the Fe^{3+} ions that accumulate in the course of the reaction due to the decomposition of ferroin and ferriin; however, this does not correspond to actual wave dynamics of the medium.

5. Other reactions

Propagation of a single reaction front can also be observed in non-oscillating chemical systems, *e.g.*, in those characterised by rather large initial concentration gradients. The use of gels with high content of water allows one to suppress convection and, at the same time, permits experimental procedures typical of liquid-phase NMR studies to be employed for imaging using the proton signal of water. In particular, diffusion-controlled redox processes were studied using a hollow, thick-walled cylinder made of polyacrylamide gel saturated with aqueous $Fe_2(SO_4)_3$ solution at pH 1.[32] Filling the cylinder cavity with aqueous sodium bromate solution (pH 1) causes diffusion of the reagent into the cylinder walls and, as a consequence, oxidation of Fe^{2+} to Fe^{3+}. In the presence of Fe^{3+} ions the T_1 time of the water protons is shortened to a much greater extent compared to the Fe^{2+} ions. Because of this, T_1-weighted NMR images obtained at different stages of the process exhibit a noticeable increase in the amplitude of the signal of water present in the cylinder walls as a result of propagation of the reaction front towards the outer surface of the cylinder.

In another series of experiments Fe^{3+} was reduced to Fe^{2+} with an aqueous ascorbic acid solution (pH 1), which led to a decrease in the signal amplitude. An identical cylinder made of polyacrylamide gel was used to obtain the 2D NMR image of the copper ion release process occurring upon variation of the pH value of the medium.[33] First, the material the cylinder was made of was doped with a chelate complex of copper with ethylenediaminetetraacetic acid. Then the cavity of the cylinder was filled with a sulfuric acid solution (pH 1.2). Proton diffusion into the bulk of the gel caused protonation of the ligand present inside the walls of the cylinder and shifted the complexation equilibrium towards the formation of free copper ions. In the presence of a chelate copper complex the T_1 time of water is shortened to a much lesser extent than in the presence of free Cu^{2+} ion due to poor contact of copper and the hydration shell. Therefore, the formation of free Cu^{2+} ions led to substantial enhancement of the NMR signal of water in the T_1-weighted images. Analysis of a set of 1D profiles acquired during the propagation of the reaction front along the axis of the continuous cylinder showed that the displacement of the reaction front is proportional to the square root of the time, which is typical of a diffusion process.

Introduction of calcium ions into aqueous sodium alginate solution [34] causes cross-linking of the alginic acid molecules by calcium ions, resulting in the formation of a rigid gel. As a consequence, the T_2 time of the water molecules is shortened from 0.8 to 0.1 s. In the experiments sodium alginate and the solution of calcium ions were separated by a dialysis membrane. The process was studied with planar and cylindrical geometries at different concentrations of the reagents by acquiring the 1D and 2D NMR images. It was found that the reaction front moves in proportion to $t^{1/2}$ (t is time) and the diffusion coefficient of calcium ions depends on the concentration of calcium (due to different pore sizes and electrostatic interactions in the gel).

Gelation can be reversed by adding an aqueous solution of a sodium salt of ethylenediaminotetraacetic acid, since the acid favours removal of calcium owing to the formation of chelate complexes.[35] Depolymerisation-induced changes in the molecular mobility cause substantial variations of the spin–lattice relaxation times of the water molecules (T_{1sat}), measured at external saturation of the nuclear magnetic resonances of gel macromolecules, as a result of magnetisation transfer. This served as the basis for monitoring the movement of the sol/gel interface along the axis of a cylindrical sample during gel destruction. A combination of a 1D 'null-point' technique (here, the NMR signal of water molecules with prescribed time T_1 becomes zero due to incomplete magnetisation recovery after inversion) with selective saturation of the resonance signal from macromolecules was employed. The authors suggested that the process is controlled by diffusion transport of the acid towards the sol/gel interface. This technique allows one to selectively follow the movement of the region with any pre-selected gel concentration, since the T_{1sat} time depends on the local concentration of gel. An increase in the initial gel concentration causes the moverment of the sol/gel interface to slow down.[35]

Studies of reactions in the solid phase require the use of solid-state NMR spectroscopy techniques. An anisotropic acid–base reaction of substituted benzoic acid with ammonia gas was investigated using a multipulse line-narrowing technique that allowed elimination of the dipolar coupling and chemical shift effects to second order.[36] The authors expected that

2D T_1-weighted images of the molecular single crystal will correspond to very slow conversion of 4-bromobenzoic acid into ammonium 4-bromobenzoate on the (100) crystal face, where the carboxylic group is less accessible compared to other faces. However, the experiments revealed only weak anisotropy; this was rationalised by the poor quality of the crystal. In another experiment ammonium gas was blown over a thick layer of powdered toluic acid to give ammonium toluate. Using a series of 1D MRI projections acquired at different times, the authors showed that deeper layers of the acid sample begin to react later and at a lower rate than do the surface layers. Both experiments were carried out with the proton T_1 time governing the image contrast, since the T_1 time of the initial acid was much longer than the T_1 time of the reaction products.

A feature of some photoinduced radical reactions in solutions is the effect of chemically induced dynamic nuclear polarisation (CIDNP), or the nonequilibrium population of nuclear spin sublevels in the reaction products due to the spin dynamics in the short-lived radical pairs.[37, 38] As a result, the NMR signal of the reaction products can be substantially enhanced and even change its sign in the case of population inversion. Spatially resolved studies of this effect observed during the UV photolysis of *tert*-butyl methyl ketone in CCl_4 revealed spatially inhomogeneous variations of the signal amplitude in the sample due to inhomogeneous light absorption.[39] Intense irradiation of the sample initiated mixing of the solution. A possible reason is convection owing to heating of the sample.

Hydrogenation of unsaturated compounds with dihydrogen with nonequilibrium ratio of molecules with different total nuclear spin (ortho- and para-hydrogen) can cause dramatic enhancement of the NMR signal of the reaction product.[40, 41] Variation of the magnetic field can be used for polarisation transfer from the ^1H to the ^{13}C nuclei in the reaction product.[42] In particular, this allowed an angiogram of a living rat to be generated in 0.9 s after introducing the reaction product in the caudal vein.[43] The experiments were carried out at the natural abundance level of the ^{13}C isotope (1.1%) and the NMR signal enhancement due to the polarisation of the ^{13}C nuclei was 10^4.

Figure 3 presents the 2D images acquired during catalytic decomposition of hydrogen peroxide on a cylindrical catalyst granule (Pt/Al_2O_3) 3.6 mm in diameter. Figure 4 illustrates the capabilities of NMR imaging for studying the liquid phase distribution inside a catalyst granule during the evaporation of

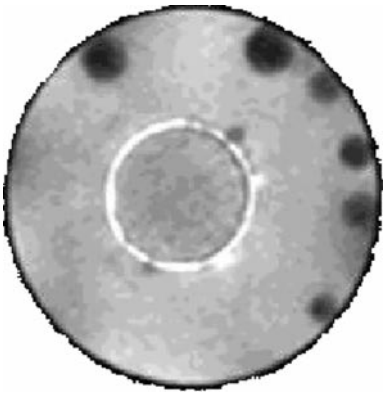


Figure 3. A 2D NMR image of a cylindrical ampoule filled with a H_2O_2 solution. A catalyst granule (Pt/γ-Al_2O_3) is located at the centre of the ampoule.
Clearly seen are the gas bubbles formed on the ampoule walls and on the surface of the catalyst granule. A bright circle surrounding the catalyst granule corresponds to the domain with a strong NMR signal due to a decrease in the T_1 time in the near-surface region.

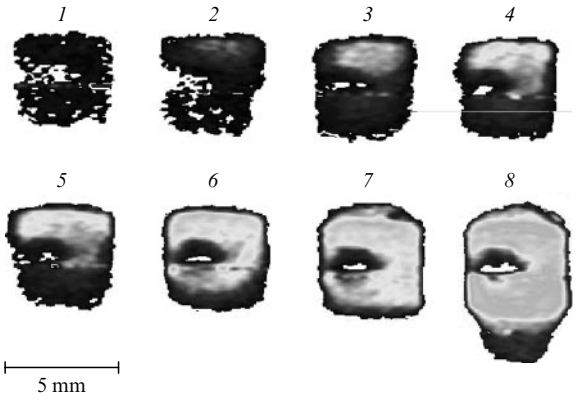


Figure 4. Liquid phase distribution inside a Pt/γ-Al_2O_3 granule during the evaporation of AMS accompanied by its vapour-phase hydrogenation.
The supply of liquid AMS increased from 0 to 0.71 mg s^{-1}. The temperature of the granule /°C: 109 (*1*, *2*), 141 (*3*), 167 (*4*), 148 (*5*), 113 (*6*), 100 (*7*) and 64 (*8*). Brighter regions correspond to a higher content of liquid. The formation of an AMS droplet under the catalyst granule can be seen in the image (*8*).

α-methylstyrene (AMS) accompanied by its catalytic hydrogenation.†

III. Magnetic resonance thermometry

Variable-temperature NMR studies allow one to obtain a much greater body of information; however, this requires reliable methods for measuring the temperature of samples. In some experiments, this can be done using a thermocouple. However, this technique can introduce errors into the results of the NMR experiments. Pulsed field gradients induce eddy currents, thus increasing NMR signal distortion. In addition, variation of the geometry of the object under study in the presence of a thermocouple affects the temperature field distribution over the entire sample. Finally, experiments in nonzero magnetic fields can make the results of temperature measurements less reliable.

The NMR technique provides a means for using the molecules of the object under study as thermal sensors to measure the temperature inside the object. There is a set of reference samples for which the temperature dependencies of the chemical shift, linewidths or their splittings in the NMR spectra have been studied in detail. In particular, methanol and ethylene glycol serve as references in the case of ^1H NMR spectroscopy; these compounds are used in different temperature ranges.[44]

A new era in the development of magnetic resonance thermometry is associated with the possibility of using the NMR imaging technique for constructing the spatial temperature distribution maps, which is of particular interest for biology and medicine. For instance, low-temperature hyperthermia involves heat treatment of tissues at elevated temperatures (43 – 45 °C) during tens of minutes either to kill malignant cells or to enhance their susceptibility to cytotoxic agents and/or irradiation. To induce necrosis of tissues due to protein denaturation after short-term heat treatment, even higher temperatures (50 – 80 °C) are used.[45] At 43 °C, 100% necrosis occurs in several tens of minutes.[45, 46] On further increases in temperature the time taken to necrotise tissues nearly halves as the temperature increases by 1 °C

† See I V Koptyug, A V Kulikov, A A Lysova, V A Kirillov, R Z Sagdeev, V N Parmon *Dokl. Akad. Nauk* **385** 205 (2002) [*Dokl. Phys. Chem. (Engl. Transl.)* **385** 158 (2002)]; I V Koptyug, A V Kulikov, A A Lysova, V A Kirillov, V N Parmon, R Z Sagdeev *J. Am. Chem. Soc.* **124** 9684 (2002).

and reaches ~ 1 s at 57 °C.[45] NMR imaging allows real-time assessment of temperature-induced variations in tissues in the course of thermal therapy procedures, which can be used for feedback creation in automated systems.[47] MRI also allows visualisation of changes in tissues after the completion of the therapeutical procedure. In addition, by using open-design devices one can also monitor the position of the applicator during the insertion in tissues.[48]

NMR-Assisted temperature measurements are based on the fact that such parameters as the molecular diffusivity (D), nuclear magnetisation (signal amplitude), spin relaxation times and the resonance frequency of a nucleus (chemical shift) are sensitive to the local temperature. The characteristic temperature sensitivity of these parameters for tissues in living organisms and corresponding phantom objects in the physiological temperature range are of the order of 0.8%–2% $(^\circ C)^{-1}$ for T_1, 2.4% $(^\circ C)^{-1}$ for D, -0.007 to -0.01 ppm $(^\circ C)^{-1}$ for the chemical shift of water molecules[49] and ~ 0.01 ppm $(^\circ C)^{-1}$ for both the ^{19}F nuclei in fluorinated hydrocarbons and ^2D nuclei (see Refs 50 and 51). The ^{13}C and ^{59}Co nuclei are also used.[51] For Co(III) compounds the temperature coefficient of the chemical shift is 1.5–3 ppm $(^\circ C)^{-1}$. Similarly to other types of experiments, the main problem of these studies is to select the temperature-induced contribution to overall variations of the parameters investigated. Therefore, methods based on variation of the NMR resonance frequency, which is less sensitive to side processes, are usually employed.

Many experiments have been carried out using the so-called proton resonance frequency (PRF) technique based on the resonance frequency variation when recording the ^1H NMR spectra of, *e.g.*, water. Temperature-induced variations of the water proton resonance frequency are mainly due to variation of the shielding constant caused by the cleavage, stretch or bending of hydrogen bonds.[52] There is a linear correlation between the chemical shift of water and the temperature at least up to 80 °C. The advantage of the PRF technique is a constant value of the corresponding temperature coefficient for many samples, which was demonstrated in the studies of phantom objects and various types of tissues *in vivo*[52] and *ex vivo*.[45] Low sensitivity can be compensated by mapping the phase of the magnetisation instead of acquiring the resonance frequency variations.[53–56] To correct the phase of the signal (in particular, to include the magnetic field drift), the object under study is often surrounded by reference samples that are kept at room temperature.[57–59] If a number of signals with comparable amplitudes is observed (in, *e.g.*, water–fat systems), the chemical shift selective phase mapping allows one to avoid phase measurement errors for the total NMR signal and provides an internally referenced measurement tool (to this end, the signal of, *e.g.*, fat can be used).[60] In some instances acquisition of a complete NMR spectrum is followed by numerical simulation to exactly determine the resonance frequencies.[61, 62]

In practice, the situation is complicated by the fact that the local magnetic field depends not only on the chemical shift, but also on the magnetic susceptibility of the sample, which in turn is a function of temperature. If temperature-induced variations of the volume magnetic susceptibility are large, variation of the local resonance frequency is not proportional to the local temperature and is determined by the temperature distribution over the entire sample.[63] In this case the heat source geometry and orientation in the magnetic field are of great importance.[64] In contrast to water, typical of fat is a relatively small temperature-induced variation of the resonance frequency, which is mainly due to local variations of the diamagnetic susceptibility rather than chemical shift.[53] On the one hand, this hampers temperature measurements in fatty tissues,[58] but, on the other hand, allows the fat tissue signal to be used as a reference,[52, 60, 61] which can be of value in measuring the absolute temperature. However, it should be noted that magnetic susceptibility variations in fatty tissues can distort the local fields and introduce errors when measuring temperature in neighbouring muscle tissue.[63] For this reason one should also avoid the use of paramagnetic substances (conventional water dopants for thermostatting the object under study).

Other sources of errors in tissue temperature measurements can be:[52, 58, 61, 65] low signal-to-noise ratio, limited spectral resolution, inhomogeneity of the magnetic field, variation of the magnetic field due to eddy current magnetic field, field drift, variation of tissue perfusion and oxygen concentration in blood and temperature-induced variation of the magnetic susceptibility of tissues. Position shift, as well as a change in the size or geometry of the object under study (*e.g.*, muscles) can introduce rather large errors into the results of temperature measurements.[52, 66–68] The drawbacks of the technique is low spatial and temperature resolution.[52] Despite this fact the temperature map can be obtained using the proton phase shift imaging technique even on an open-configuration, low-field (0.2 T) scanner with a rather large field drift during the experiment.[69] The error of measurements can be less than 0.5 °C for temperature variation by 10 °C.[52]

Stollberger *et al.*[70] reported separate measurements of the temperature coefficients of the diamagnetic susceptibility and chemical shift for water, gel, brain tissue and fat tissue. Both numerical simulation and test experiments showed that the contribution of temperature-dependent magnetic susceptibility to the variation of the NMR resonance frequency depends on the orientation of the laser applicator and on the distance from the applicator and can be large, especially for tissues with high fat content. In contrast to other authors, experiments with a human calf muscle revealed no effects due to variation of the diamagnetic susceptibility of fat.[57] At the same time, a complex response of living tissues to temperature variation was pointed out. The NMR signal of water in a living organism can be affected by both blood flow and magnetic susceptibility variations due to the change in the concentration of paramagnetic substances, *e.g.*, the oxy/deoxy state ratio of hemoglobin and myoglobin in blood. As a result, the temperature dependencies of the NMR signal parameters have the shape of hysteresis curves.[57]

De Poorter[63] evaluated the relative contributions of the temperature dependencies of the chemical shift and magnetic susceptibility to the temperature dependence of the proton resonance frequency in agarose gel and in porcine muscle tissue and fat tissue. In the experiments cylindrical gel samples were oriented both parallel and perpendicular to the magnetic field direction. The relative temperature-induced change in the magnetic susceptibility of fat tissue was shown to be close to the relative variation of the chemical shifts in muscle tissue and agarose gel. The temperature coefficients of the chemical shift in fat tissue and of the magnetic susceptibility in muscle tissue and gel appeared to be very small.

Temperature distribution studies during the heating of a rat hindleg[58] and cooling of a human leg[61] (5–37 °C) using a water jacket have been reported. It was found that the temperature decreases to a greater extent in the regions with a thinner layer of fat tissue. The results obtained suggested that the cooling–heating cycle was accompanied by muscle deformation and/or muscle position shift.[58] Spatial temperature distributions were also monitored in the course of interstitial magnetic resonance-controlled laser-induced thermal therapy of head and neck tumours,[71] human brain tumours[54] and during microwave-induced interstitial heating and thermal lesions in rabbit brain *in vivo*.[55] The methods employed were often tested on phantom objects (*e.g.*, agarose gel[58]); however, calibration of the water proton chemical shift for practical thermal surgery was carried out *in vivo* for ultrasound-heated rabbit tissues.[72]

Fast MRI techniques allow mapping the temperature distribution in 1–2 s.[56] Two-dimensional temperature maps for water-heated agarose gel were obtained in fractions of a second with an accuracy of 0.2 °C.[73] The temperature distribution over the sample was calculated by converting the phase change relative to the initial NMR image acquired at the known temperature using a calibration curve.

NMR spectra exhibiting several signals with different chemical shifts allow internal-referenced (or self-referenced) temperature determination by measuring the chemical shift differences between two particular NMR lines.[62] This approach was illustrated by the experiment with a double cylinder filled with ethylene glycol. The inner part of the cylinder was microwave heated. The local temperature in the sample was determined from the chemical shift difference between the OH and CH_2 groups of ethylene glycol molecules (the corresponding temperature dependencies are well known). A feature of an *in vitro* study of a porcine liver sample placed in a vessel filled with continuously heated water was the use of the effect of temperature on the chemical shift difference between the proton signals of lipids (polymethylene chain, $-CH_2-$) in water and in liver; the time for acquiring 2D temperature maps varied from 10 s to 3 min. The authors pointed out that, in contrast to other methods involving voxel-by-voxel comparison of two NMR images, their self-referenced method is less sensitive to translational motion of the sample in the course of the experiments.[62]

Nott *et al.*[53] reported on mapping the temperature distributions induced in food by heating to 120 °C and even higher temperatures. To confirm that the changes in the signal phase were due to the variations of the temperature of the sample, additional experiments were carried out with a vessel containing pre-heated homogeneous gelated suspension of starch which was allowed to cool. The temperature distribution maps obtained revealed clearly seen radial temperature gradients in the vessel. In the experiment with less viscous agar gel the temperature distribution map was significantly distorted by stochastic convection effects. Food sauce was chosen as an example of an heterogeneous medium. The chemical shift was shown to be insensitive to structural inhomogeneities of the sample. The experiments provided data on both temperature distribution over the sample and structural inhomogeneity, which allows suggestions about interrelations between heat transfer processes and the structure of the product. The temperature dependencies of the spin relaxation times and diffusion coefficients have also been reported.[53]

The possibility of acquiring separate NMR images of the volumes of water kept at different temperatures using the chemical shift difference between water protons was demonstrated taking two ampoules filled with water heated to 32 and 75 °C as an example.[74] The same study also reported separate NMR images of three coaxial cylinders containing an inorganic phosphate solution with different pH values (12, 7 and 3) obtained with the ^{31}P NMR signal detection.

The chemical shifts of atomic nuclei in paramagnetic complexes are usually much more temperature sensitive compared to the chemical shifts of nuclei in diamagnetic compounds. In addition, the former substantially differ from the latter in magnitude, which allows one to avoid the overlap of lines in the NMR spectrum. For instance, the temperature sensitivity of the chemical shift of ^{1}H and ^{31}P nuclei in a thulium complex with a macrocyclic cycloaza ligand is 0.89 ppm $(°C)^{-1}$ for the former and 2.18 ppm $(°C)^{-1}$ for the latter nucleus (two orders of magnitude higher than for water protons).[75] A method of simultaneous measurements of the temperature and the pH value of the medium using this paramagnetic thulium complex has been proposed.[76] This approach was practically implemented for the measurement of the temperature within the sample when thermostatting the NMR probe or applying heteronuclear decoupling and was based on measuring the resonance frequency difference between two lines in the ^{1}H NMR spectrum of the water-soluble thulium complex.[77] In principle, the technique allows temperature variations of the order of 0.01 °C to be measured.

The advantage of a paramagnetic praseodymium complex is the large proton chemical shift (−24.1 ppm) relative to the conventional values.[78] The temperature sensitivity of the chemical shift, −0.131 ppm $(°C)^{-1}$, is independent of both the pH value of the medium ($5.6 \leqslant pH \leqslant 9.6$) and the concentration of the complex. The possibility of using the complex was demonstrated in the *in vivo* experiments with rat liver. Yet another advantage of paramagnetic complexes is the short T_1 times of the magnetic nuclei. Aime *et al.*[79] developed a paramagnetic complex Yb–DOTMA [DOTMA is ($\alpha,\alpha',\alpha'',\alpha'''$)-tetramethyl-1,4,7,10-tetraazacyclodecane-1,4,7,10-tetraacetic acid] and studied its behaviour in human blood serum. They found that the chemical shift of the most intense line from four Me groups is −14.2 ppm, the temperature coefficient is 0.04 ppm $(°C)^{-1}$ and that the chemical shift difference between a prescribed pair of spectral lines is even more temperature sensitive [−0.42 ppm $(°C)^{-1}$].

Another method of temperature measurements is based on the temperature dependence of the spin relaxation time T_1. For many types of tissues the T_1 time of water protons is a nearly linear function of the temperature in the range between 20 and 50 °C. However, the temperature coefficients of T_1 for different tissues are also different and therefore a preliminary calibration and knowledge of the chemical composition of tissues to be studied are required.[65] In addition, living organisms respond to temperature variations in a complex manner, so that the relation between T_1 and the temperature can be nonlinear.[80] Nevertheless, it was found that the temperature coefficient of the T_1 time is 13 ms $(°C)^{-1}$ ($T_1 \approx 1$ s) for sheep mammary glands and 3.2 ms $(°C)^{-1}$ ($T_1 \approx 360$ ms) for fatty tissues.[81]

A temperature distribution study using a fast T_1 mapping technique has been carried out with an agar-gel cylinder in which a radial temperature gradient was created.[82] A calibration curve for converting the local T_1 values into temperature was obtained.

Signal amplitude in the T_1-weighted image can also serve as a measure of temperature distribution over the sample. In this case one should take into account the fact that a decrease in the signal amplitude with an increase in temperature is a consequence of both the increase in T_1 and the decrease in the equilibrium magnetisation. To construct the temperature map, one should acquire the NMR image of the sample at ambient temperature and have a calibration curve, $T_1(T)$, for a particular type of tissue or use known data for this type of tissues. This method was used for construction of the temperature map in muscle tissue heated by placing the tissue in contact with a heated glass tube or by deposition of focussed ultrasound energy.[83] In the latter case the focal spot was inside the tissue, which was clearly seen in the NMR images acquired (region with very low signal intensity). All experiments were carried out at 20–45 °C. The difference between the MRI data and the temperature values measured using fibre-optic probes was at most 0.6 °C. The technique was also implemented in studies of the temperature distribution in gel or bovine muscle tissue *in vitro* or in rabbit muscle tissue *in vivo* during focussed ultrasound therapy treatment.[84, 85] The focal spot size and the thermal diffusivity were determined.[85] It was shown that temperature variation in the axial direction was asymmetric and that the near-field zone was heated to higher temperatures than the far-field zone. The near-field zone also cooled slower than the focal spot, which can lead to overheating upon repetition of ultrasound pulses.

Inversion–recovery T_1 measurements for a flowing fluid can be complicated since flow can cause additional changes in the signal amplitude.[86] It was proposed to create an inverted signal in a set of slices separated by slices with equilibrium nuclear magnetisation rather than in the entire sample. In this case the signal amplitude in the non-inverted regions in the immediate vicinity of the slice with inverted magnetisation can be used for normalising the signal amplitude. This approach is similar to the tagging technique employed in the studies of fluid flows;[2] single experiments additionally allow one to obtain information on the character of the flow. The method was implemented using a model comprising two tubes, a tube through which water was pumped (T = 40.2 °C at the inlet) and an external jacket through which a fluorinated cooling agent was pumped in a parallel direction (T = 9.8 °C). A 2D temperature distribution map was obtained. The accuracy of measurements was 15% of the temper-

ature difference between the inlet and outlet (which was equal to15 °C).

The T_1 time of solid *cis*-polybutadiene at room temperature is 16 ms. This allows observation of the NMR signal of the polymer.[87] Based on the results of T_1 measurements, a temperature map was obtained for a *cis*-polybutadiene block through which cold (10 °C) and hot (70 °C) water was pumped using two tubes. The temperature coefficient of T_1 was $\sim$ 12 ms (°C)$^{-1}$ at the T_1 times ranging from 0.2 to 0.8 s. The maps obtained exhibited reasonable agreement with the results of calculations.

Local temperatures can also be determined from the molecular diffusion coefficients. Temperature variations upon heating of a polyacrylamide gel with an RF hyperthermia applicator were monitored using the 2D map of the diffusion coefficient of water molecules.[88] The local temperatures determined from the images averaged over a volume of 1 cm^3 were found to be in good agreement with those recorded using implanted fibre-optic probes or a thermocouple (the difference was 0.2 °C). Temperature-related changes in the NMR signal intensity of agarose gel and rabbit brain tissue *in vivo* irradiated by a Nd : YAG laser were visualised by acquiring diffusion-weighted 2D images in 150 ms.[89] This method was also employed for *in vivo* temperature measurements of a human calf muscle.[90] The authors pointed out that the regional blood volume decreased by a factor of 3.5 on cooling and increased by a factor of 2.7 on heating as the temperature varied by several degrees.

A number of comparative studies of the above-mentioned temperature measuring techniques has been reported. Bertsch *et al.*[65] implemented and evaluated two methods based on the chemical shift and T_1 relaxation measurements taking external heating of samples in the range 22 – 50 °C using a water jacket and local (focal) laser heating in the range 22 – 35 °C as examples. MRI data were then compared with the results of fibre-optic temperature readings. The chemical shift method is usually more convenient than T_1 relaxation measurements for constructing more accurate 2D temperature distribution maps in shorter times. In agarose gel, the error was 0.6 °C; however, for more heterogeneous samples the error increased to 1 – 3 °C, especially in the presence of fat. In the latter case, the T_1 relaxation method gave better results. Cline *et al.*[91] reported construction of temperature maps for heating of tissues *via* focussed deposition of ultrasound energy using simultaneous information on the chemical shift and T_1 variations (the error of measurements was 0.7 °C).

Comparison of the methods based on the chemical shift and water diffusion coefficient measurements revealed [59] higher accuracy of the former (the root-mean-square deviation was 0.1 – 0.15 °C) in the case of short-term measurements (measuring time less than 1 h) with inclusion of magnetic field drift correction (to this end, additional reference samples kept at a constant temperature in the course of the experiment were placed around the sample under study).

The sensitivity and other characteristics of the three above-mentioned methods have also been compared.[49,53] Experiments were carried out with agarose gel in the temperature range 35 – 45 °C. It was shown that only two methods, namely, those based on the water proton chemical shift and T_1 relaxation measurements, permit construction of the temperature distribution map with an accuracy better than 1 °C at 15 s acquisition time, the former being more accurate than the latter.[49] Model calculations for the three methods have been reported.[67] The necessity of taking into account tissue perfusion variation and blood flow effects was pointed out.

Other parameters of the NMR signal can also be used for temperature measurements. For instance, the 1D temperature profile along the length of the NMR ampoule thermostatted by flowing air was constructed using variation of the ^{1}H NMR linewidth of dibromomethane dissolved in a nematic thermotropic liquid crystal as a 'thermometer'.[92] It was shown that placing the NMR ampoule with the sample in a static bath (perfluorinated oil of high heat capacity) causes no decrease in the longitudinal temperature gradient but makes it more uniform and, probably, eliminates transversal temperature gradients. The dipole and quadrupole splittings in the NMR spectra of molecules dissolved in nematic liquid crystals are also temperature sensitive.[93,94] A 5% benzene solution in a nematic liquid crystal was used for temperature measurements in the range 290 – 330 K.[93] The frequency difference between the outermost spectral components varied from 7300 to 5300 Hz. The corresponding temperature coefficient increased from 52.5 Hz (K)$^{-1}$ at 296 K to 111 Hz (K)$^{-1}$ at 330 K. The linewidth can serve as a measure of the temperature field inhomogeneity within the sample.

The operating temperatures of cryosurgery can be as low as −180 °C. Obtaining information on the temperature distributions in frozen tissues using NMR spectroscopy seems to be highly improbable. Nevertheless, NMR imaging can be used for determining the cryoprobe position upon introduction into tissues as well as the position and displacement of the phase transition boundaries.[95] This permits assessment of the temperature distribution based on solution of the equations derived from inclusion of thermal conductivity, metabolism and blood flow effects.

MRI also allows imaging of frozen tissues during and after defrosting.[96]

In conclusion, NMR spectroscopy of various nuclei is used in measuring low and ultralow temperatures.[97,98]

IV. Magnetic resonance current density imaging

NMR imaging can be used for visualisation of static and radiofrequency magnetic fields produced within the sample by external sources.[1] In contrast to this, current density imaging (CDI) technique allows visualisation of local magnetic fields created within a sample by an electric current flowing through the sample. This permits calculations of the spatial current density distribution over the sample. It should be emphasised that, similarly to other experiments considered in this review, the CDI method is based on acquisition of NMR signals from certain types of atomic nuclei. Therefore, the electric current density can be determined only in those regions of the sample which produce observable NMR signals.

If a direct current flows through a sample, the phase of the precessing transverse magnetisation varies in proportion to the projection of the current-induced local magnetic field on the direction of magnet's field. Experiments are carried out using direct current pulses synchronised with the NMR pulse sequences.[99,100] Generally, measurements of the three mutually perpendicular components of the local magnetic field require repetition of the experiments at three different orientations of the sample. However, usually it is sufficient to construct two-dimensional cross-sections of the spatial current density distribution maps in the plane perpendicular to the direction of the electric current flowing through the sample. To date, the sensitivity of corresponding experimental techniques, optimum current pulse duration and amplitudes [99,100] and possible artifacts [100,101] have been studied. Model experiments [99,100,102] with a cylinder filled with aqueous NaCl solution confirmed theoretical conclusions. More rigorous tests of experimental methods involved measurements of the three spatial components of the electric current density around a spherical volume of the solution placed at the centre of the cylinder and encapsulated in an insulating sphere.[101] The results obtained were in good agreement with the MRI data and current density calculations. The measured magnetic field amplitudes obeyed Maxwell's equations. The distribution of direct current flowing through plant stem fragments (*Pelargonium zonale, Rosa arvensis*) pre-soaked in a 10% saline solution in order to enhance the conductivity has been studied.[99]

Electric current through a fragment of a hen thighbone immersed in physiological saline containing Gd – DTPA (DTPA is diethylenetriaminepentaacetic acid) has been studied in order to study osteoporosis and to evaluate the feasibility of electrical

stimulation of bone tissue growth to recover damaged regions in the case of bone fracture.[103] Changes in the current density upon artificial demineralisation or mechanical damage were visualised. The magnitude and spatial distribution of the current density are of great importance for electrotherapy and electrochemotherapy of tumours. Mice tumours and the effects of electrode geometry on the electric current distribution within the tumours have been studied.[104] Joy *et al.*[102] detected a change in the signal phase in the NMR image of the cross-section of a human forearm (one of the authors of the study[102] volunteered) in the experiments with application of a 2 mA electric current (pulse duration was 40 ms) flowing from the elbow towards the wrist.

Yet another possible application of the CDI technique is the investigation of chemical reactions and other physicochemical processes which are accompanied by changes in the electrical conductivity due to changes in the local concentration of ions (*e.g.*, dissolution of a NaCl crystal in agar gel[105]). The current density maps obtained revealed an increase in the concentration of mobile ions in gel followed by diffusion-induced redistribution of the ions during the dissolution of the crystal. The NMR images allowed changes in the size of the crystal to be monitored, which is NMR silent in contrast to the surrounding gel and looks at the region with very high noise level. The current density imaging technique was also employed to study the formation and subsequent dissolution of calcium carbonate.[105] Diffusion of carbon dioxide through a membrane into the bulk of agar gel doped with a saturated calcium hydroxide solution resulted in insoluble calcium carbonate. As a result, the conductivity of the sample reduced due to a decrease in the concentration of calcium ions and hydroxide ions. The dynamics of gas diffusion into the gel bulk was monitored by inhomogeneity of the conductivity within the sample. Further treatment of the gel with gaseous hydrogen chloride, which reacted with calcium carbonate to give soluble calcium chloride, led to recovery of gel conductivity.

Alternating currents flowing through samples at the Larmor frequency are studied by the RF–CDI method.[106, 107] The RF field component with circular polarisation in the plane perpendicular to the external magnetic field affects the magnetisation analogously to the RF field of the spectrometer. The corresponding pulse sequence includes the alternating current pulse coherent to other RF pulses. Usually, the proton decoupling channel is used in the experiments with ^{1}H nuclei. Under particular conditions (*e.g.*, in the experiments with cylindrical geometry) all the necessary components of the current-induced RF field can be determined at a single orientation of the sample. Further data processing allows mapping not only of the alternating current density, but also of the current phase which depends, in particular, on the relative contributions of the conduction and displacement currents. An RF–CDI study of a plastic cylinder filled with $CuSO_4$-doped aqueous NaCl solution has been reported.[106] Unambiguous determination of the matrix describing the rotation of the magnetisation vector during the current pulse requires a series of experiments at different initial orientations of the magnetisation vector (this extends the measuring time).

Similar to the above-mentioned method of mapping direct current density distribution is the rotating frame RF–CDI approach proposed to study alternating current density distributions.[108] In this case the current pulse is applied simultaneously with the RF pulse created by the transmitter coil. If the coil field amplitude is sufficiently large, only the projection of the current-induced field on the direction of the RF field of the spectrometer contributes largely to the nutation of the magnetisation vector. Scott *et al.*[108] reported the analysis of the problems concerning the finite amplitude and inhomogeneity of the RF field of the spectrometer as well as artifacts and of the sensitivity analysis. Trials have been performed using a three-compartment cylindrical model object containing an aqueous NaCl solution doped with $CuSO_4$ (mainly the conduction current was detected), a $CuSO_4$ solution (detection of the displacement current) and a mineral oil (no current was detected). In addition, the spatial distribution of the current density and phase in the cross-section of a rat body *ex vivo* was obtained and the feasibility of the imaging procedure with tissue-dependent contrast (due to the electrical properties of biological tissues) was demonstrated. The experiments were carried out at 85.6 MHz.[106, 108] It was pointed out that the technique can also be useful for the determination of the absorbed dose rate in the case of RF pyrotherapy and NMR imaging. The RF–CDI method was also employed in studies of the dynamics of changes in the brain conductivity of a living rat upon a decrease in the membrane potential due to the introduction of kainate into a lateral ventricle of the brain.[109] An increase in the alternating current density at a frequency of 100 MHz was mainly observed in the hippocampal area. Kainate affects the central nervous system inducing epilepsy; therefore the results of these experiments demonstrate the feasibility of the technique for studies of epileptic attacks and the action of antiepileptic pharmaceuticals.

Both CDI and RF–CDI investigations were mostly carried out at current densities ranging from 25 to 2500 A m^{-2}, however, theoretical estimates[100] suggest the possibility of measuring current densities of the order of 0.1 A m^{-2}.

Electric current can also be induced by the piezoeffect intrinsic in various animal and plant tissues and by neuronal firing. Taking a model sample (isolated copper conductor immersed in an aqueous NaCl solution doped with copper sulfate) as an example, the feasibility of detecting phase changes of the proton NMR signal images was demonstrated.[110] The phase change detected corresponded to a change in the magnetic field by a value of 1.7 nT, which is equivalent to simultaneous firing of nearly a million neurons.

Finally, mention should be made that the magnetic field of electric current can be measured not only in the laboratory frame, but also in a moving frame of reference if the NMR signal is detected using the nuclei of the ions creating the electric current through the sample.[111]

V. NMR imaging of gases

1. General remarks

The sensitivity and resolution of the MRI techniques employed in studies of gases is usually much lower as compared to fluids, since the gas density is three orders of magnitude lower than the density of water under normal conditions. In addition, for many gases efficient spin-rotational interactions cause the relaxation time T_2 ($T_2 \approx T_1$) to fall in the millisecond range[112] and be shorter than the minimum time needed to create the echo signal, which leads to a considerable loss of signal. Finally, the diffusion coefficients of gases at atmospheric pressure are 4–5 orders of magnitude higher than the self-diffusion coefficient of water. A decrease in the NMR signal amplitude due to stochastic molecular motion in inhomogeneous magnetic fields is well known and serves as the basis for a widely used method of measuring diffusion coefficients using NMR.[2] Since the imaging procedure requires the use of magnetic field gradients, fast gas diffusion causes further reduction of the signal-to-noise ratio. In addition, gas diffusion imposes limitations on the achievable spatial resolution, which cannot be better than the characteristic distance of the diffusion displacements of molecules over the time taken for spatial localisation of spins. High diffusion coefficients of gases can be the reason for substantial distortion of NMR images due to the edge enhancement effect.[2]

Fortunately, there are some ways to partially overcome these difficulties. Short relaxation times T_1 of many gases (SF_6, CF_4, C_2F_6, CH_4) allow multiple accumulation of the NMR signal over a relatively short time to improve the signal-to-noise ratio.[112–114] In addition, the spin relaxation times of these gases are virtually insensitive to the presence of dioxygen and solid surfaces.[113] Moreover, sometimes the relaxation times of gas molecules in porous media can increase due to frequent collisions of the gas molecules with the walls and/or due to the surface adsorption.[115, 116] By recording the free induction decay (FID) or

implementing various versions of the single-point imaging technique (SPI, SPRITE) it is possible to compensate the loss of signal due to short relaxation times T_2 and fast diffusion [112] or flow effects.[117]

The spin relaxation times of relatively large gas molecules can approach those typical of many liquids. For instance, the relaxation times of butane are $T_1 = 1.27$ s and $T_2 = 0.75$ s at 1 atm and room temperature. Long relaxation times T_2 allow signal acquisition over a long period of time including multiple refocussing of the echo signal to improve the sensitivity or implement rapid imaging techniques. In addition, large molecules have smaller diffusion coefficients (for propane, $D = 6.6 \times 10^{-2}$ cm^2 s^{-1} at 22 °C).

Experiments with molecules containing a large number of magnetic nuclei (*e.g.*, SF_6, C_4H_{10}) also permit improvement of the sensitivity of NMR imaging. In this case possible differences between the chemical shifts of nuclei are insignificant, since the chemical shift difference between inequivalent groups of atomic nuclei is often not resolved due to substantial line broadening. High adsorption of gases by porous materials also leads to substantial enhancement of the signal (Fig. 5); therefore, NMR imaging of adsorbed gases can be employed for measuring the local adsorption isotherms. By increasing the gas pressure one can increase the spin concentration and spin relaxation times and reduce the diffusion effects. However, this faces some problems, *e.g.*, one should use thick-walled ampoules or specially designed probes, an increase in the gas pressure can damage brittle samples (this also causes an increase in not only the relaxation time T_2, but also T_1, which requires the duration of the experiment to be extended due to the necessity of lengthening the relaxation delay between the pulse sequence repetitions).

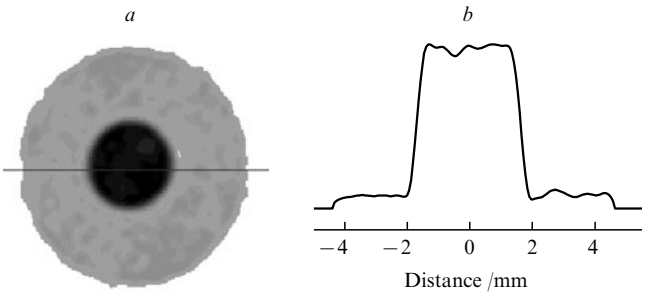


Figure 5. A 2D NMR image of the cross-section of a butane-filled cylindrical ampoule 10 mm in diameter with an alumina granule inside (*a*) and a 1D section of the NMR image (*b*); due to adsorption of butane the amplitude of the NMR signal from the alumina granule is an order of magnitude higher than the signal amplitude from the surrounding butane gas.

Another method of improving the sensitivity of NMR, which has recently gained wide acceptance, is the use of hyperpolarised gases [118] for which the population difference between the spin sublevels much exceeds the equilibrium population in the magnetic field of a spectrometer. This is achieved using non-radioactive isotopes ^{129}Xe and ^{3}He (for both the nuclear spin is 1/2). There are two approaches for creating the nonequilibrium population of nuclear spin sublevels. One involves optical pumping of the D1-transition of the optical absorption of rubidium vapours at a wavelength of 794.7 nm (the use of cesium can be even more efficient). Irradiation with circularly polarised light creates a nonequilibrium population of one of the two electron spin sublevels in the magnetic field and then the rubidium electron spin polarisation is collision transferred to the nuclear spins of noble gases. This technique allows one to achieve a 30% of polarisation of gas (in this case the signal of the gas at a pressure of 1 atm is an order of magnitude more intense than the ^{1}H signal of a water sample of the same volume). Often, mixtures of xenon and other gases (N_2, ^{4}He) are used at the natural abundance level of the ^{129}Xe isotope (26.44%) or using isotope enrichment. The natural abundance of the ^{3}He isotope is very low (1.3×10^{-4} %); therefore, experiments are carried out only with isotopically enriched samples.

The other method for polarising the nuclear spins of ^{3}He involves optical excitation (at a wavelength of 1083 nm) of metastable helium states created in the gas discharge, followed by collisional transfer of the nuclear polarisation to the ground state. Pumping occurs at a gas pressure of about 10^{-3} atm and then the pressure is increased to the operating values.[119] Yet another method of NMR signal enhancement by a factor of 100 involves storage of helium at 2–4.2 K in a strong magnetic field (several T) followed by transfer in the magnetic field of the spectrometer and heating to room temperature.[120]

Unlike many other gases, spin-rotational relaxation of monoatomic noble gas molecules is often inefficient due to spherical symmetry of the electron cloud; therefore, the spin relaxation times of these isotopes are rather long.[121, 122] NMR studies of nonpolarised noble gases are often carried out using their mixtures with oxygen to substantially reduce the relaxation time T_1.[123, 124] On the contrary, in the experiments with hyperpolarised gases long relaxation times T_1 allow one to appreciably extend the lifetime of the nuclear polarisation, which permits polarised xenon to be obtained in the solid, liquid [125] and supercritical [126] states and its transportation over long distances. Phase transitions cause no considerable loss of the spin polarisation while depolarisation of liquid xenon is insignificant even in the weak geomagnetic field.[125] Long relaxation times T_2 allow multiple refocussing of the magnetisation and acquisition of a large number of echo signals during each repetition of the pulse sequence.

Application of RF pulses causes irreversible loss of spin polarisation.[127, 128] Therefore, experiments are designed in such a way that the loss of polarisation occurs portionwise due to the use of low-flip pulses. In some experiments the flip angle is gradually increased after each pulse as the longitudinal magnetisation decreases.[129] Fast gas diffusion can partially compensate the loss of magnetisation owing to the polarised gas present outside the slice under study.[130] A number of experimental setups has been designed to permit 'on-the-fly' polarisation of the ^{129}Xe nuclei up to 3% and thus to provide continuous circulation of the hyperpolarised gas through the sample and fast recovery of the magnetisation destroyed by the RF pulses.[117, 131–133]

The nuclear magnetisation of hyperpolarised nuclear spins is independent of the applied magnetic field, B_0. In this case the signal-to-noise ratio is proportional to B_0 instead of B_0^2 under the equilibrium polarisation conditions (see Ref. 134). Therefore, experiments with hyperpolarised gases are particularly efficient when operating in weak magnetic fields [135, 136] that are used in, *e.g.*, biomedical studies. Lower magnetic fields cause substantially lower field gradients due to the difference between the volume magnetic susceptibility of materials and, hence, considerable reduction of NMR image distortion and the signal decay rate ($1/T_2^*$). In addition, one can use lower field gradient amplitudes, simpler and cheaper MRI scanners and operate at lower resonance frequencies. This causes an increase in the thickness of the skin layer for conducting materials and makes it possible to study, *e.g.*, gases in metallic containers, which cannot be done in strong-field experiments.

High spin magnetisation of hyperpolarised gases was shown [134] to induce radiation damping effects [137–140] (the so-called RF maser effect [141]). In particular, placing a helium-filled cell (2.5 atm, 15% polarisation) into an RF coil in a homogeneous magnetic field caused fast spontaneous loss of polarisation despite the low Q-factor ($Q = 10$) and low filling factor (2%) of the RF coil.[135] Similar effects can introduce errors into the experimental results. After acquiring the NMR signal the magnetic field gradient pulses destroy the transverse magnetisation, thus weakening the radiation damping effects.[134]

2. Gases with equilibrium nuclear polarisation

Despite the above-mentioned difficulties accompanying NMR imaging of gases, interesting results have been obtained in a number of studies using gases with equilibrium nuclear polarisation at both elevated and normal pressure. Rinck *et al.*[142] seem to report a pioneering study concerning NMR imaging with gas signal acquisition. They studied dog lungs using a $CF_4 - O_2$ [80 : 20 (vol.%)] mixture and ^{19}F NMR signal acquisition in a weak magnetic field (938 G). The frontal, sagittal and transversal NMR images of the lung volume revealed poor ventilation of the upper part of the left lung induced by pneumonia. Considerable promise of the application of physiologically inert perfluorinated gases in real-time studies of perfusion and lung ventilation in stronger magnetic fields was pointed out. [142]

A $C_2F_6 - O_2$ (80 : 20) mixture was used for forced ventilation of rat lungs. Lungs were imaged with a spatial resolution of 700 μm at 4.3 h acquisition time.[114] The fluorine relaxation times at a rat body temperature of 39 °C were $T_1 = 5.9$ and $T_2 = 5.3$ ms. Two-dimensional NMR images of rat lungs were also obtained with a spatial resolution of 4.4 mm by acquiring a total of 64 successive echo signals of thermally polarised ^3He in 8 min.[143]

Varying the concentration of oxygen in gas mixtures allows one to reveal regions of lungs with low alveolar ventilation-to-blood perfusion ratio.[113] These regions are characterised by an increased relative concentration of the blood insoluble gas (a two- or threefold increase if gas mixtures with high concentration of oxygen are used). NMR imaging experiments with a $SF_6 - O_2$ mixture with different component ratios demonstrated a marked difference between the images of a normal rat lung and the lung partially blocked by inserting a glass bead with a lumen into the left bronchus.[113]

The SPRITE technique was employed to acquire a 1D NMR image of a methane-filled cylindrical glass ampoule divided by Teflon disks into cylindrical layers 2 and 3 mm thick and a 3D image of a fragment of the *Diploria labyrinthiformis* coral placed in a rubber balloon filled with SF_6 at a pressure that was somewhat higher than atmospheric pressure.[112] In the latter case the relaxation times ($T_1 = 1.8$ and $T_2^* = 0.6$ ms) were shorter than for pure SF_6 ($T_1 = 2$ and $T_2^* = 1$ ms at 1 atm), which was attributed to the interaction of gas with the developed surface of the porous sample.

The opposite trend was observed in studies of CF_4 and C_2F_6 in the pores of a layered composite ceramic material similar to mullite in chemical composition.[115] The relaxation times T_1 of both gases in the pore space of the sample at gas pressures of 0.5 to 5 atm exceeded those of the bulk phase gases by more than an order of magnitude and became much less pressure dependent. The relaxation times T_2 exhibited similar changes. The decrease in the relaxation rate can be rationalised by the adsorption of gases and by reduction of the rotational correlation time of the molecules at small pore sizes, where the frequency of collisions with the ampoule walls becomes comparable with the frequency of intermolecular collisions. The 2D NMR images demonstrated the layered structure of the sample, delamination regions and inner voids. Considerable changes in the spin relaxation times, spin density and effective diffusion coefficient of the gas in the pore space ($D = 6 \times 10^{-3}$ cm^2 s^{-1} for the bulk phase C_2F_6 gas at 5 atm and 295 K and $D = 10^{-4}$ cm^2 s^{-1} for gas occluded in pores of the sample) allows the use of these parameters as the basis of the image contrast related to the characteristic dimensions of the morphology and to the local values of the specific surface of the pore space. In particular, an increase in the amplitude of the field gradients used for image acquisition causes suppression of the signal of the gas outside of the sample and allows selective visualisation of gas within the pore space characterised by relatively slow diffusion.[115] The surface adsorption of C_2F_6 and C_4F_8 was also observed in studies of partially sintered, tetragonal Y-stabilised zirconia powders.[116] The sample porosities were determined based on the results of relaxation time measurements.

Intercalation of AsF_5 into highly oriented pyrolytic graphite was studied using fluorine-detected NMR imaging.[144] The concentration of AsF_5 uniformly increased with time throughout the sample. After equilibration, the diffusion coefficients of the fluorine atoms involved in the exchange processes were measured.

Studies of the structure of mesoporous silica-based material (M41S) showed that the pores in the sample with strongly disordered structure are almost inaccessible to xenon, whereas the samples with more ordered structure exhibited the presence of physisorbed xenon.[145] The experiments revealed fast exchange of xenon in the interparticle space with physisorbed xenon.

Variation of the chemical shift of ^{129}Xe over a wide range (300 ppm depending on the environment) in combination with various selective NMR imaging techniques[1] permits chemical shift selective MRI investigations using the ^{129}Xe atoms in a particular environment. For instance, Gregory *et al.*[123] studied silica aerogel samples sealed in an ampoule filled with xenon (30 atm). The NMR images acquired using the lines at $\delta = 46$ and 52 corresponded to ^{129}Xe in aerogel, while the images acquired using the line at $\delta = 17$ allowed visualisation of the volume of the ampoule around aerogel.[123] In addition, it was found that optically transparent and translucent samples correspond to different chemical shifts of the ^{129}Xe lines, thus indicating considerable differences in the pore structure of these samples. Shorter relaxation time T_2 points to smaller pore size in the translucent samples characterised by a lower concentration of ^{129}Xe. Two-dimensional NMR images of the periphery of aerogel revealed regions containing almost no xenon due to mechanical breakdown of pores.[123] The sensitivity of the chemical shift of adsorbed ^{129}Xe to the presence and concentration of co-adsorbates was used in diffusion studies of the adsorbed water in NiNaY zeolite at 100 °C.[146]

The ^{131}Xe quadrupole nucleus with a spin of 3/2 can be more sensitive to the character and state of the surface of a material, despite a smaller gyromagnetic ratio and a lower natural isotope abundance compared to the ^{129}Xe nucleus. A study of liquid xenon in mesoporous aluminosilicate aerogels at 285 K (this temperature is close to the critical temperature, 289 K) showed that the chemical shift and especially the spin relaxation times of ^{131}Xe depend on the density of the aerogel.[147] In addition, ^{131}Xe in the regions outside of aerogel is characterised by a different chemical shift value and longer relaxation time T_1, which allows selective suppression of the NMR signal from the environment. It was also shown [147] that the relaxation time T_1 of the ^{131}Xe isotope in the gel changes upon removal of the adsorbed water, whereas the relaxation times of ^{129}Xe remain unchanged. The results obtained demonstrated considerable promise of the use of quadrupole relaxation of the ^{131}Xe nuclei as a sensor in studies of the state of various surfaces and of the presence of non-paramagnetic substances on the internal surface of the pores.[147]

3. Hyperpolarised gases

The potential of NMR imaging of hyperpolarised gases has been demonstrated using a number of phantom objects. For instance, NMR images of $^3He^*$ (3 atm) in a glass cell [134] and of $^{129}Xe^*$ in capillary tubes [130, 131] or in nested glass tubes (with a spatial resolution of ~0.1 mm) [130] have been reported. Hyperpolarised gas flow was also imaged.[131] NMR images of a cylindrical aerogel sample revealed the presence of regions with characteristic millimetre-scale dimensions, which are hardly accessible to xenon.[130]

Using chemical shift selective MRI of a sample of NaY zeolite powder in a porous glass tube, separate NMR images of xenon gas, xenon in NaY zeolite and xenon in porous glass were obtained.[117] Separate NMR images of xenon in NaY and CaA zeolite granules were also acquired based on the difference in pore size and in the nature of the cation. All the experiments were carried out at a total gas mixture pressure of ~1 atm using a continuous flow of hyperpolarised xenon for continuous renewal of the spin polarisation within the sample and demonstrated the possibility of real-time investigations of the adsorption of xenon.[117]

Transport of xenon towards the inside of SiO_2 aerogels or spherical zeolite 13X granules was studied by acquiring separate NMR images of bulk phase xenon ($\delta = 130$) and xenon occluded in pores ($\delta = 25$).[133] When a continuous flow of the gas is used, the reduction of xenon polarisation by the RF pulses can be utilised to selectively observe the signal of the fresh, inflowing portion of gas. Therefore, by varying the repetition time of the pulse sequence one can obtain NMR images corresponding to different penetration depths of xenon in the porous sample. Experiments with aerogel at long pulse repetition times revealed a homogeneous distribution of hyperpolarised xenon over the sample. For zeolite, fast spin relaxation of xenon occluded in pores allowed acquisition of the Xe NMR signal only from a narrow near-surface region of the granules. The signal amplitude rapidly decayed towards the granule centres. Both samples exhibited obstructed penetration of xenon into the granules in the areas of close interparticle contact and near the walls of the sample container.[133]

Long spin relaxation times of xenon and helium are convenient for diffusion studies[2] and provide the possibility of studying molecular displacements at times as long as several tens of seconds.[148] Diffusion coefficient measurements have been reported for ^{3}He* in a glass cell[121] ($D = 1.8$ cm^2 s^{-1} at 1 atm) and in a glass cylinder,[149] as well as for ^{129}Xe* in a glass sphere[129] ($D = 0.057$ cm^2 s^{-1} at 1.04 atm). Investigations of transport of hyperpolarised xenon towards the inside of a porous glass sample permitted the determination of the diffusion coefficient of adsorbed xenon ($D = 2.2 \times 10^{-8}$ cm^2 s^{-1} at 293 K) and the activation energy for diffusion (4–5 kJ mol^{-1}).[127] A continuous-flow system was used in studies of ^{129}Xe* diffusion in narrow channels of nanoporous crystallites.[148] The temporal dependence of the NMR signal corresponded to a 'single-file' diffusion.

Using the cross-polarisation (CP) or spin polarisation induced nuclear Overhauser effect (SPINOE) techniques, the polarisation of xenon can be transferred to adjacent nuclei including the nuclei of the atoms of a solid surface.[150–154] In particular, CP studies of the transfer of xenon polarisation to protons of polymer films[155] or to the surface of bulk polymer samples[156] have been reported. With a continuous flow system Seydoux and Pines[151] studied the polarisation transfer from the ^{129}Xe* nuclei to the surface protons of aerosil. The CP technique is more efficient on less mobile atomic groups, whereas SPINOE works better with more mobile ones. The CP ^{1}H NMR spectrum exhibited a broad polarised line, while a much narrower signal was observed in the SPINOE experiment. By using the CP technique the proton polarisation thus obtained can be transferred to the ^{29}Si nuclei. In addition, direct SPINOE-induced polarisation transfer from the xenon nuclei to the ^{29}Si nuclei causes enhancement of the ^{29}Si NMR signal from the surface atoms by a factor of 20 to 30.

Navon *et al.*[150] also reported the nuclear polarisation transfer of ^{129}Xe* dissolved in benzene to the solvent protons. Due to the low efficiency of the cross-relaxation mechanism the maximum enhancement factor of the ^{1}H signal varied from 10% (for C_6H_6) to 50%–200% for a C_6D_6–C_6D_5H (3 : 1) mixture. The dynamics of changes in the 2D images of the ^{129}Xe* signal in the ampoule suggested that initially the dissolved xenon is accumulated in the bottom region of the ampoule rather than at the open upper end contacting the bulk gas phase. This is due to an increase in the fluid density upon the dissolution of xenon. The NMR images obtained using the signal from the solvent protons were in good agreement with those obtained by acquiring the ^{129}Xe signal. This demonstrates the possibility of indirectly mapping the spatial distribution of xenon and studying the properties of the medium through which xenon penetrates.

Most publications have been concerned with applications of hyperpolarised gases in biomedical studies and, first of all, in studies of pathologies of respiratory organs. Experiments on animal and human lungs are usually carried out with ^{3}He* for which one can obtain a higher nuclear spin polarisation.[122] In addition, the polarisation can last over a long period of time due to very long relaxation times T_1 ($\sim$100 h under normal conditions).[157]

Hyperpolarised ^{3}He was used for imaging rat lungs[134] and guinea pig lungs[157] *ex vivo*. In the latter case helium also penetrated into the myocardium (because of the use of a large volume of gas). Experiments with living guinea pigs[158–160] showed that the chemical shift of ^{3}He in their lungs is sensitive to the volume magnetic susceptibility of the surrounding tissues.[161] This can be employed in studies of the microstructure of lungs and of various lung pathologies.

Helium was used in studies of rat lungs *in vivo*,[162] human lung parenchyma,[119, 160, 163–166] upper respiratory tract[164] and paranasal sinuses.[167] Experiments were carried out on healthy volunteers and patients with various lung diseases diagnosed using conventional methods.[168, 169] The different abilities of helium and air to penetrate into partially blocked regions of internal organs have been pointed out.

The possibility of functional imaging of lungs by acquiring a set of 2D images of ^{3}He* in different stages of the respiratory cycle with a temporal resolution of 50 ms has been demonstrated taking guinea pigs as examples.[170] Using fast imaging techniques (acquisition times 40–120 ms) allows real-time studies of the ventilation dynamics of human lungs during one respiratory cycle.[136]

To optimise the NMR parameters, the diffusion coefficients and the T_2^* relaxation times of ^{3}He* and ^{129}Xe* in lungs of a living guinea pig were measured.[171] The relaxation time T_2^* of ^{3}He* in human lungs was also determined.[172] It was found that the diffusion coefficients of these gases in lungs are 3–10 times lower than in the trachea due to geometric restrictions on the molecular diffusion displacements and to different amounts of residual air.[171] The T_2^* relaxation time in lungs is also shorter due to rather large local inhomogeneities of the magnetic field and the presence of the residual air.[172]

Acceleration of the relaxation of ^{3}He* in the presence of oxygen can be used for measuring the local partial pressure of O_2 as a function of time.[173] This was demonstrated taking measurements of the partial pressure of oxygen in a phantom object with the known oxygen concentration as an example. Analogous *in vivo* studies of ^{3}He* in porcine and human lungs revealed a linear decrease in p_{O_2} with time upon breath holding. The error of measurements of p_{O_2} was $\sim$3%. The concentration of oxygen in lungs strongly depends on gas exchange, regional blood flow and oxygen uptake; therefore, this experiment offers new possibilities of studying lung work and diagnosing lung diseases.

The spin relaxation time T_1 of xenon gas is of the order of tens of minutes. This is much shorter compared to helium but sufficient for the use of xenon for NMR imaging of lungs. In addition, the T_1 and T_2 relaxation times of xenon are very sensitive to the environment and can be employed as the basis of image contrast agents.[122] Xenon was used in, *e.g.*, the *in vitro* studies of forced ventilation of lungs on mice lungs (different stages of the filling of a lung were investigated),[174] lungs of a living mouse during unobstructed breathing[175] and lungs of a living rat.[176] Intensive research has also been carried out on volunteers; in particular, NMR images of lungs[177] and the oral cavity[178] have been obtained.

Guinea pig lungs were studied *in vivo* to compare the NMR images obtained using hyperpolarised xenon and helium.[179, 180] Helium allows acquisition of high-quality images at higher spatial resolution.[180]

At the same time, xenon also has some advantages over helium. It has high solubility in blood and various tissues and binds strongly to proteins. The solubility of xenon in blood and lipids is one and two orders of magnitude higher than that of helium, respectively.[122] A study of the dynamics of changes in the NMR signal revealed rapid transport of xenon gas from lungs into the vascular system,[181] which permits investigations of blood circulation in the organism and in various organs.[177] The spin

relaxation time T_1 of ^{129}Xe dissolved in blood strongly depends on the concentration of oxygen in blood due to the change in the interaction of xenon with hemoglobin ($T_1 = 4$ s in the absence of oxygen and 6.5 – 13.5 s in oxygen-saturated blood [182, 183]). Taken together with good solubility of xenon in lipid-rich brain structures, this can be used as a promising technique for functional MRI, which is based on the variation of regional cerebral blood flow upon regional activation, and for investigations of the mechanisms of the action of anesthetics on living organisms.

In vivo experiments on rats showed that a fraction of the nuclear polarisation of $^{129}Xe^*$ survives transport from lungs to blood and then through myocardium to the brain.[184] Two-dimensional NMR images of xenon in brain tissue were obtained using the difference between the chemical shifts of xenon gas and xenon dissolved in tissues and blood. The signal from cerebellum was less intense than the signal from the cerebral hemispheres, which can be due to different blood flow velocities. Further experiments revealed four xenon resonances in the rat organism,[181] which were attributed to bulk phase xenon gas and to xenon dissolved in blood, fat and tissues. Different chemical shifts of xenon in plasma and erythrocytes have been reported.[183] By combining the spatial resolution of the NMR images and spectral information it was possible to follow the transport of $^{129}Xe^*$ from rat lungs into lung parenchyma and pulmonary blood, and then with blood flow through heart ventricle into myocardium, brain and kidneys.[181]

Model estimations [128] showed that after intracarotid injection of a $^{129}Xe^*$ solution the peak concentration of Xe* in the brain will be several times higher compared to Xe* transport through lungs. Specific features of xenon delivery to tissues by intravenous injection of a xenon solution compared to xenon respiration have been documented.[122] The potential and drawbacks of various biocompatible solvents for delivery of xenon to blood and tissue using xenon solution injection have been reported.[185] The spin relaxation times of xenon in various environments have also been measured.[122]

Rat hindleg was imaged using intramuscular injection of xenon dissolved in saline.[128] Fresh human blood in an ampoule was imaged after addition of a xenon solution in an aqueous suspension of lipid vesicles.[185] Intrinsic exchange of xenon between erythrocytes and the plasma – saline mixture has been studied.[185] Intravenous injection of xenon dissolved in a 30% soya oil-in-water emulsion into the tail of a living rat with simultaneous acquisition of MR angiograms of the abdominal and pelvic veins was used [186] for visualisation of the vascular system (MR angiography [2]). This allowed selective imaging of relatively large veins and estimation of the velocity of blood flow through them. In contrast to proton MR angiography, the xenon-based technique does not require the elimination of the signal of immobile nuclei.

Compared to xenon, the solubility of helium in blood and biocompatible solvents is 10 – 100 times lower, which poses some problems. To overcome them, a suspension of hyperpolarised ^3He microbubbles in a biocompatible fluid (Hexabrix) was introduced into the caudal vein or the aorta of a living rat to provide visualisation of the venous and arterial system, respectively.[187] In the preliminary stage (prior to injection) the effective spin relaxation time T_1 of xenon in suspension was 42 s and partially reflected the loss of the signal due to rapid rise of bubbles out of the suspension. Hand-agitated suspension contained relatively large bubbles (mean bubble diameter was 31.8 μm and the standard deviation was 10.4 μm). A narrower size distribution centred at 8 μm, which can be achieved by modern techniques, seems to be more preferable. This would provide safe transport of bubbles through the pulmonary circulation and obviate the risk of embolism. The amount of suspension (7 ml or 25% of the total rat blood volume) can be substantially reduced due to an increase in both the concentration of bubbles and the polarisation of helium nuclei. A possible application of this approach is the quantitative assessment of blood circulation in myocardium.

VI. Magnetic resonance imaging of solids

The main problem of the MRI studies of solids is that the lines in the NMR spectra of solids are 3 to 5 orders of magnitude broader than those in the NMR spectra of liquids. For instance, the linewidth in the NMR spectrum of polyethylene depends on the properties of the material and varies between 20 and 60 kHz.[188] This imposes severe restrictions on the achievable spatial resolution. In addition, broad lines correspond to a short signal decay time, which substantially reduces the sensitivity. On the other hand, the decay time can be lengthened using various procedures for creating the spin echo signal in a solid material.[189] Molecular diffusion in solids is usually insignificant and has no effect on the spatial resolution of the technique.

From the standpoint of NMR, the so-called 'soft' solid materials such as polymers and elastomers occupy an intermediate position between liquids and 'hard' solid materials. That is, they are characterised by linewidths ranging from 100 to 3000 Hz and contain a large number of protons.[189] Therefore, 'soft' materials can sometimes be studied by the above-mentioned experimental methods. The spectral lines can be narrowed by increasing the mobility of macromolecules as a result of an increase in temperature or swelling of the material in a solvent.[190, 191] For instance, heating of a polypropylene block to 330 K substantially improves the signal-to-noise ratio in the 2D NMR image.[4] In the case of 'rigid' materials a high degree of orientational ordering and low concentration of the isotopes of the nuclei under study can substantially reduce the contribution of the homonuclear dipole – dipole coupling to the linewidth.[189]

There is a number of methods for efficient eliminations of various types of interactions which contribute to the linewidths in the NMR spectra of solids.[188, 189, 192, 193] For instance, the magic-angle spinning (MAS) technique is widely used to suppress the chemical shift anisotropy. In this case the imaging procedure requires synchronisation of the rotating (or pulsed) field gradients with the sample rotation. Magic-angle spin-lock allows averaging of anisotropic interactions without mechanical rotation of the sample.[194] Decoupling with composite pulses permits suppression of heteronuclear dipolar spin coupling while various multipulse techniques are used for suppression of homonuclear dipolar couplings and for line narrowing up to three orders of magnitude.[195, 196] In particular, a signal dephased due to homonuclear dipole – dipole coupling can be rephased using the magic echo pulse sequence.[188, 197] By combining the magic echo pulse sequence and the CPMG pulse sequence to eliminate the chemical shift effects the adamantane NMR line was narrowed from 13 kHz to 3 – 8 Hz.[196, 198]

The so-called constant time imaging (CTI) techniques involve obtaining spatial information by phase encoding of the signal. Because of this, the linewidth does not impose limitations on the spatial resolution. For instance, the single point imaging (SPI) technique [1, 199, 200] involves measurements of the FID amplitude at a single point 10 – 100 μs after application of the RF pulse, which allows studies of objects with short relaxation times T_2, and T_2^* (gases, solid materials and samples with large internal magnetic field gradients). Such gradients are typical of, *e.g.*, samples with numerous interfaces between phases with different magnetic susceptibilities (porous media, animal and plant tissues, *etc.*). In the SPI technique, the signal at the centre of the k-space ($k = 0$) is acquired at a zero external field gradient, so that diffusion causes no additional loss of the signal even in the studies of fluids and gases. Nevertheless, the signal-to-noise ratio decreases due to short relaxation times T_2 and T_2^*. SPI experiments with the phase encoding of the NMR signal instead of the frequency encoding elongate the image acquisition times.[1] In some instances the SPI method is employed in combination with fast imaging techniques (*e.g.*, the turbo spin echo SPI technique).[201] This approach was used, in particular, for investigating heterogeneous samples including hardened cement. The SPRITE technique [1] is a

version of the SPI procedure, which also allows considerable reduction of the measuring time.[202–206] It has been used in studies of various materials including cement, concrete, bone tissues, rigid polymers and gases with short spin relaxation times (including H_2).

Often, for short-T_2 materials acquiring the FIDs rather than echo signals provides a means for improving the sensitivity of the experimental technique. Therefore, in some instances the NMR images are reconstructed using a method similar to X-ray computerised tomography. The technique is based on recording the FID in the presence of a magnetic field gradient and multiple repetition of the experiment at different directions of the field gradient. The results obtained (1D projections) are then used for reconstruction of 2D or 3D NMR images from the projections using relevant software.[192] Continuous-wave MRI can also offer some advantages over the pulsed techniques in studies of materials with submillisecond relaxation times T_2.[207]

Broad-line effects on the spatial resolution can be eliminated using large-amplitude field gradients. NMR probes have been developed, which permit creation of pulsed field gradients up to 60 000 G cm^{-1} (see Ref. 208). Finite inductance of gradient coils and the eddy currents induced in conducting materials cause the gradient switch on/off time to extend, thus shortening the minimum achievable echo time. In this situation one can use sinusoidal field gradients and a gradient coil incorporated into the resonant circuit.[209–211] In this case, the RF pulses are applied at the instant when the gradient passes through zero. Using a doubly resonant coil, one can adjust the shape of the field gradient in such a way that it has an inflection point at zero, which permits an increase in the duration of the RF pulse, thus improving NMR image quality.[211,212] Oscillating field gradients allow reduction of the echo time down to $\sim$100 μs. For instance, a 3D image of a plastic LEGO® brick has been obtained (characteristic relaxation time T_2 of the material was 760 μs).[209,212]

A number of stray field imaging (STRAFI) [1] studies have been reported.[213–217] The method involves placing the NMR probe in the region where the magnetic field amounts to *ca.* 40% of the maximum magnetic field value but the field gradient can exceed 10 000 G cm^{-1}. At such gradient amplitudes, even a short RF pulse affects nuclear spins only within a narrow slice of the sample. 1D STRAFI images are obtained by mechanically moving the sample along the field gradient direction through the sensitive slice. Stepwise rotation of the sample permits 2D and 3D NMR imaging. The method allows studies of samples with metallic inclusions and of paramagnetic materials.[218] Using an additional coil, one can vary the magnetic field, thus displacing the sensitive region within the limits of 1 cm without moving the sample.[219]

Multiquantum NMR imaging involves creation of a coherence in the system of interacting spins (nth order coherence; $n > 1$).[220] The evolution frequency of the multiquantum coherence is n times higher than the Larmor frequency of spin precession ($n = 1$) in the magnetic field. Because of this, at $n = 10–20$ the effective amplitude of the field gradients employed increases by an order of magnitude during acquisition of NMR images.[221]

Using selective pulses for slice selection and chemical shift selective imaging also face some difficulties, since the pulse duration can exceed the signal decay time in solid materials.[221] Application of large field gradients permits slice selection with short RF pulses (several microseconds). Slice selection can also be achieved by spin-lock in the presence of a field gradient [210] and by selective saturation of the nuclear magnetisation outside the slice under study due to long relaxation times T_1 in solid materials. The above-mentioned line narrowing techniques allow the use of long pulses and pulse sequences for selection of a particular slice or spectral line.[189] Some other slice selection methods have been developed.[222–224] Heteronuclear polarisation transfer [225] between, *e.g.*, the ^{1}H and ^{13}C nuclei offers considerable promise for selection of a particular group of atomic nuclei in multicomponent systems.

Short, large-amplitude RF pulses that are used in solid-state NMR studies require high RF power. This imposes limitations on the size of the sample (usually, the sample is no larger than 1 cm). Samples that can be as large as one likes (*e.g.*, the Earth) are studied using surface coils [226] or a device which combines the RF coil and the magnetic field source. Local studies of the properties of large samples can be performed with a surface scanner ('NMR Mouse'), which is suitable for exploring almost any solid materials [227,228] including metal-supported polymeric coatings, human skin and tendons, *etc*. Small size and weight make the device mobile. Because of this the spectrum of possible applications of the method is broadened and includes, in particular, studies of aircraft wings, auto-tyres reinforced with steel-wire cord, buildings, bridges and conveyer belts.[10] The device comprises two permanent magnets and a surface coil which produce a static and an RF field in the near-surface layer of the sample. Inhomogeneity of the fields produced defines the size of the sensitive volume (characteristic dimensions are 4×9 mm at a thickness of 0.5 to 1 mm). By varying the frequency of the alternating field the sensitive zone can be displaced over a distance of 0 to 5 mm from the surface. An additional gradient coil allows 1D spatially resolved NMR imaging within the field of view (15 mm) without mechanically moving the probe.[229]

An NMR image can be obtained using radiofrequency field gradients (B_1-imaging technique) in combination with static magnetic field gradients or instead of them.[192] The advantage of this approach is insensitivity to static magnetic field inhomogeneities typical of heterogeneous samples.

Feasibility of using MRI techniques to obtain information on solid materials (including real-time monitoring of technological processes) is of considerable interest in spite of technical problems and complexity of practical implementation. The major advantage of NMR imaging is the possibility of targeted variation of image contrast by choosing appropriate pulse sequences. It is this feature that allows one to collect information on the structure and state of the samples and processes occurring in them. This also holds for solids. Using theoretical and empirical relationships, one can estimate such characteristics of materials as the degree of homogeneity, the dynamics and degree of molecular ordering, chemical composition, molecular velocities and reaction rates, mechanical stress and deformations, degree of cross-linking of polymers, filler agglomerate distribution, ageing, temperature, viscosity, *etc*., from the quantities measured experimentally (*e.g.*, relaxation times, chemical shifts, linewidth and lineshape). The most important procedures for creating image contrast in solids and methods of practical implementation have been well documented.[230–232] Only a few examples are presented below.

NMR imaging of solids is most widely used in studies of polymers and elastomers (Figs 6 and 7). In particular, MRI experiments revealed the presence of inhomogeneously distributed spherical microvoids of different sizes in cross-linked poly(isobutylene–*p*-methylstyrene–*p*-bromomethylstyrene) terpolymer.[190,191] It was found that the concentration of microvoids correlates with the mechanical properties of the material. In particular, high concentrations of microvoids can cause early destruction of the material under mechanical stress.

The relaxation times are often used as the basis of image contrast. The T_2 and $T_{1\rho}$ values (see Ref. 1) are sensitive to the cross-linking density of polymers (the latter allows characterisation of the size of defects and the molecular dynamics of the polymer).[233] The relaxation time T_2 nearly linearly decreases with an increase in the cross-link density, linearly increases with temperature and depends on the degree of tension of the sample.[188] This permitted studies of the local cross-link density in elastomers (including those during vulcanisation processes).[10,188,234] Spatial inhomogeneity of cross-linking of the polymer chains in a composite sample of butadiene–styrene rubber was investigated by measuring the effective relaxation time T_1.[235] The degree of cross-linking and orientational ordering of macromolecules can be determined from measurements of

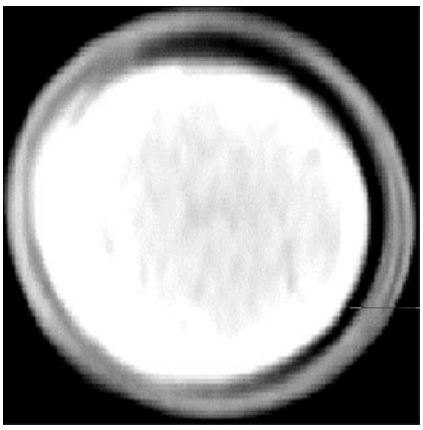


Figure 6. A 2D NMR image of the cross-section of a porous cylindrical alumina granule saturated with cyclohexane. The image was obtained using the spin echo technique.
A sealing tape (bright ring around the granule) was wrapped around the granule.

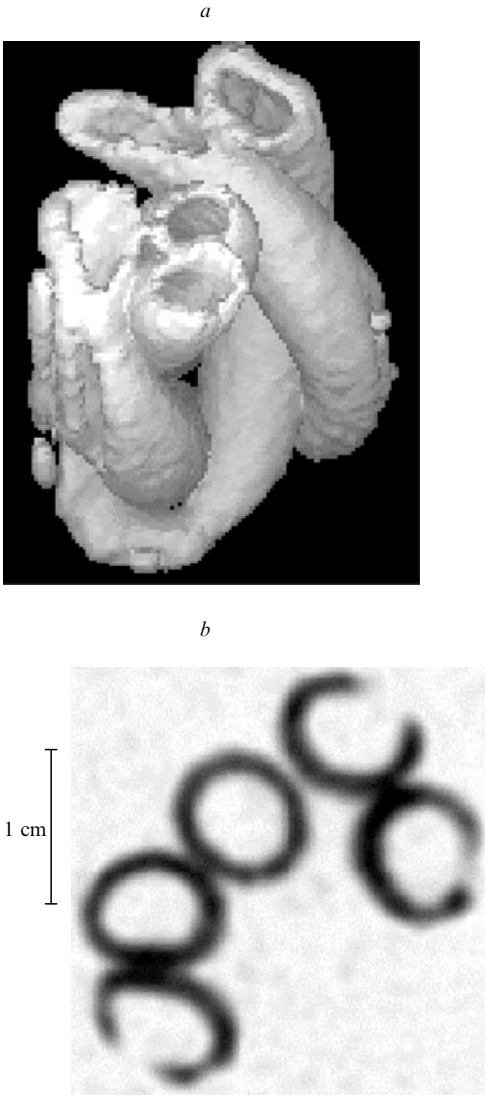


Figure 7. 3D surface rendering (*a*) and a horizontal section (*b*) of a polychlorovinyl tube tied in a bundle.
The NMR images were obtained using the spin echo technique.

residual dipolar spin–spin coupling.[236, 237] Chemical shift anisotropy was used as the basis of image contrast in a study of the ordering of pre-stressed polytetrafluoroethylene[238] and in monitoring the propagation of mechanical stress during crack growth in the material.[188] The density of cross-links between polymer chains can be determined *via* swelling of the materials in solvents.[1, 2]

The relaxation times T_2 and $T_{1\rho}$ are sensitive to slow molecular motions and suitable for studying changes in the mechanical properties of polymers and elastomers including vulcanisation and ageing.[10, 188] The results of real-time monitoring of vulcanisation of butadiene–styrene rubber without filler and with carbon black additive have been reported.[10, 11, 188] Co-vulcanisation of composite materials has been studied.[10] A study of oxidative ageing of butadiene–styrene and natural rubbers at elevated temperatures[239] revealed the formation of a rigid 'crust' on the surface of the samples. The 'crust' was shown to thicken with time.[10, 188] It was separated from the unmodified material by a narrow region characterised by increased molecular mobility due to the polymer chain scission. The influence of external conditions and chemical composition of materials on the ageing and solvent transport in aged rubbers has been studied.[240]

Mechanical ageing can be due to crystallisation induced by mechanical stress or to additional cross-linking or scission of molecular chains upon an increase in temperature. Mechanical ageing has been studied taking samples cut from a tyre as examples.[10] Inhomogeneous vulcanisation can induce early degradation of rubber items under the operating conditions. NMR images of swollen items reveal distinctions in the degree of vulcanisation between the damaged and normal regions.[188] NMR imaging also permits detection and studies of the properties of boundary regions at the interfaces between different types of rubbers upon vulcanisation.[241] A number of studies of rubber items characterised by the presence of an interface between the butadiene–styrene and natural rubbers have been carried out.

Knowledge of the distribution of mechanical stress and strain in polymeric and elastomeric items under the operating conditions is of great importance. NMR imaging provides a means for studying the changes in the molecular mobility and orientation of the molecular chains. For 'soft' materials this information can be obtained by directly measuring the molecular displacements.[2] In addition, the spin relaxation times, chemical shift anisotropy, quadrupole splittings and multiquantum coherence are sensitive to stress and deformation. The morphology of cold-drawn polycarbonate was studied [188, 242] using the effective relaxation time T_2 related to the local mobility of polymer chains as contrast agent. Measurements of the effective relaxation time T_1 permitted the determination of the mechanical stress distribution in a glass-supported tripropylene glycol diacrylate film 0.9 mm thick. It was also shown that the stress substantially increases as the distance from the film region under study to the support decreases.[235] Crack growth in polymer samples was studied by inducing tensile stress and monitoring the morphology and mechanical stress near the tip of the growing crack.[243]

The fact that many spin interactions are anisotropic can be useful for studying the deformation and stress anisotropy. Quadrupole splittings in the ^{2}H NMR spectra are very sensitive to alignment of the molecular chains as a result of changes in the degree of averaging of anisotropic interactions. The samples can be deuterated either during the preparation of materials or by swelling in deuterated solvents or oligomers. The latter approach was used for studying mechanical stress in strained natural rubber.[10, 244] Creation of two-quantum coherence [10, 237] of single quadrupole nuclei or interacting nuclei with spin 1/2 also offers some advantages.

Studies of the properties of various materials under dynamic load conditions are of great value. In contrast to conventional techniques, MRI allows spatially resolved studies of the properties of various materials and, in particular, mapping the temperature distribution over the sample. For instance, the relaxation time T_1

of butadiene–styrene rubber exponentially decreases with an increase in temperature, while the relaxation time T_2 is proportional to the local temperature.[10, 188, 245] An NMR probe was designed to carry out experiments under dynamic load conditions (compression or shear deformation) with frequencies ranging between 1 and 20 Hz. Experiments with a cylindrical sample at different load frequencies and different amounts of filler in the rubber revealed an increase in the temperature by 20 degrees and inhomogeneous temperature distribution over the cross-section of the sample.

Studies of polystyrene after bending strain or impact load[188, 227] and acquisition of a 3D NMR image of extruded polycarbonate can serve as examples in the case of rigid materials.[246] The study of polyethylene revealed nanometre-size transient regions between the amorphous and crystalline domains.[241] Spatial inhomogeneity of the distribution of crystalline and amorphous domains in polymeric materials was established by combining MRI data and spectral information obtained from ^{13}C NMR measurements.[247] NMR imaging was also employed to study the damaged regions in low density polyethylene upon electrical breakdown and the dendritic microvoid structures created by electrical breakdown.[241] It was found that the breakdown zone is characterised by a decrease in the size of crystalline domains and by an increase in the size of amorphous domains as a result of rapid local heating followed by cooling. ^{1}H and ^{27}Al NMR imaging was used to study solid propellants.[188]

* * *

In conclusion mention may be made of a number of reviews, monographs and books concerning the problems considered in this review. They are concerned with basic MRI principles[189, 248–250] and applications of the technique in various fields.[251–260] Another group of references are devoted to MRI studies of porous materials[252–254, 261] including fluid transport in porous media,[262, 263] problems of application of NMR and MRI in chemical technology and catalysis,[264–266] principles and examples of solid-state MRI applications[192, 210, 256, 267, 268] and NMR studies of noble gases.[269]

This review has been written with the financial support by the Russian Foundation for Basic Research (Project Nos 02-03-32770 and 00-15-97450) and the Siberian Branch of the Russian Academy of Sciences (the 'Integration' Programme Project No. 46).

VII. Supplement

Table S.1 presents additional information on the MRI studies considered in this review.

Table S.1. Applications of NMR imaging techniques.

Field /T	Nucleus	Object, process	Technique	Dimension	Spatial resolution characteristics [a]	Recording time	Ref.
–	^{1}H	polypropylene block at 300 and 330 K	spin echo	2D	128 × 128, a slice 5 mm thick	3.5 min	4
–	^{1}H	polymerisation of MMA + substituted peroxodicarbonate (0.2%) in a mould at 60 °C	the same	2D	128 × 256, a slice 4.5 mm thick	1 min	4
–	^{1}H	vulcanisation of a composite polymeric material reinforced with carbon fibre	"	2D	128 × 128, a slice 5 mm thick	1 min	4
6.34	^{1}H	water or water + $MnSO_4$ in a cross-linked poly(methacrylic acid) gel	"	2D	a slice 2 mm thick	–	6
2.35	^{1}H	copolymerisation of methacrylamide with *N*,*N*′-methylenebisacrylamide + 10% ammonium persulfate + tetramethylethylenediamine at 25 and 35 °C	"	2D	–	–	7
4.7	^{1}H	epoxy resin reinforced with carbon fibres	"	2D	128 × 128, a slice 1 mm thick	64 s	8
2	^{1}H, ^{19}F	methacrylic acid + benzoyl peroxide + *N*,*N*-dimethylaniline + 1,4-dibromotetrafluoroethylene	"	1D	256; 0.4 mm	5 s	12
2.9	^{1}H	photoinduced polymerisation of a resin containing methacrylic monomers	spin echo + STRAFI	1D, 3D	54 μm (1D); 128 × 128 × 128, (100 μm)^3 (3D)	–	13
4.7	^{1}H	photoinduced polymerisation of hexamethylene dimethacrylate + benzyl dimethyl ketal	spin echo	2D	256 × 256, (20 μm)^2, a slice 300 or 500 μm thick	–	14
–	^{1}H	1,6-hexanediol dimethacrylate + benzyl dimethyl ketal	the same	2D	256 × 128 or 256 × 256; from (11 μm)^2 to 39 × 78 μm, a slice 300 μm to 1.7 mm thick	–	15
3	^{1}H	irradiated polymer gel	"	2D	128 × 128 or 256 × 256 (234 μm)^2 or (195 μm)^2, a slice 1 mm thick	6.4 min or 6 h 49 min	16

Table S.1 (continued).

Field /T	Nucleus	Object, process	Technique	Dimension	Spatial resolution characteristics [a]	Recording time	Ref.
0.2	^{1}H	Fe(II) and Fe(III) ions in agar gel	spin echo with inversion – recovery	1D	512, a slice 0.11 mm thick	28 – 112 s	17
1.5	^{1}H	irradiated polymer gel	spin echo	2D	144×256, $(1.2\ mm)^2$, a slice 5 mm thick	4.5 min	19
1.5	^{1}H	X-ray or electron-beam irradiation of acrylamide + bisacrylamide + gelatin + water – O_2	the same	2D	256×256; $(1.17\ mm)^2$	–	20
1.5	^{1}H	X-ray irradiation of *N*,*N*′-methylene-bisacrylamide + *N*-vinylpyrrolidone + gelatin + water – O_2	"	2D	256×256; from $(1.9\ mm)^2$ to $(0.13\ mm)^2$, a slice 5 – 20 mm thick	–	21
2.3	^{1}H	B – Z reaction (oxidation of malonic acid by bromate ion + Mn ions + agarose + phosphate)	–	2D	a slice 2 mm thick	25.6 s	23
2	^{1}H	B – Z reaction (oxidation of malonic acid by bromate ion + Mn ions + agarose + orthophosphoric acid)	spin echo	2D	a slice 2 mm thick	12.8 s	24
2	^{1}H	B – Z reaction (oxidation of malonic acid by bromate ion + Mn ions + agarose + phosphate)	the same	3D	$128 \times 128 \times 128$; $(250\ \mu m)^3$	51.2 s	25
2	^{1}H	B – Z reaction (oxidation of malonic acid by bromate ion + Mn ions + agarose + orthophosphoric acid)	spin or gradient echo	2D	a slice 2 mm thick	13 s (spin echo) or 2 s (gradient echo)	26
2	^{1}H	B – Z reaction (oxidation of malonic acid by bromate ion + Mn ions + orthophosphoric acid)	spin echo	1D	–	–	27
2	^{1}H	B – Z reaction (oxidation of malonic acid by bromate ion + Mn ions)	the same	1D	256; a slice 2 mm thick	100 ms	28,30
2.4	^{1}H	B – Z reaction (oxidation of malonic acid by bromate ion + Ce, Ru or Fe ions)	spin or gradient echo	1D, 2D	a slice 2 mm thick or without slice selection	10 s (2D)	31
2.0	^{1}H	aqueous sodium alginate solution + $CaCl_2$	spin echo	1D, 2D	160 μm (1D); 256×256, $(200\ \mu m)^2$, a slice 5 mm thick (2D)	40 s (1D); 21 min (2D)	34
–	^{1}H	photolysis of *tert*-butyl methyl ketone in CCl_4	–	2D	–	–	39
1.5, 2.4	^{1}H, ^{13}C	dimethyl maleate in acetone or rat blood *in vivo*	gradient echo or spin echo	2D	64×128 or 256×256, 0.8×1.1 mm or $(0.4\ mm)^2$	0.4 – 2 s	43
1.5	^{1}H	rabbit or porcine brain, muscles, liver and kidney *ex vivo*	gradient echo	2D	256×256, $(0.78\ mm)^2$, a slice 10 mm thick	26 s	45
0.5	^{1}H	human brain tumour or human liver tumour	gradient echo	2D	256×128, 1.25×1.9 mm, a slice 4 mm thick	5 – 7 s	47
1.5	^{1}H	agar gel	spin or gradient echo	2D	64×128, 4×2 mm, a slice 10 mm thick	15 s	49
4.7	^{1}H	aqueous NaCl solution, agar, egg white, chicken muscles or cat brain *in vivo*	gradient echo	2D	128×128, $(0.67\ mm)^2$, a slice 3 mm thick	–	52
2.35	^{1}H	gelated starch suspension, agar gel, food sauce or aqueous gel based on organic hydrophilic polymer TX151	gradient echo (FLASH) technique	2D	256×64, $(273\ \mu m)^2$ or $(312\ \mu m)^2$, a slice 5 mm thick	12.8 s	53
1.5	^{1}H	human brain tumour during interstitial magnetic resonance-controlled laser-induced thermal therapy treatment	the same	2D	128×128, $(1.8\ mm)^2$, a slice 5 mm thick	8 s	54

Table S.1 (continued).

Field /T	Nucleus	Object, process	Technique	Dimension	Spatial resolution characteristics [a]	Recording time	Ref.
1.5	^{1}H	rabbit brain *in vivo* during microwave radiation induced interstitial heating	gradient echo	2D	256 × 256, (0.31 mm)^2, a slice 5 mm thick	< 20 s	55
1.5	^{1}H	porcine brain, muscles and liver *ex vivo*	the same	2D	128 × 128, (1.8 mm)^2, a slice 6 mm thick	1.3 s	56
1	^{1}H	human peripheral muscle (*musculus gastrocnemius*)	"	2D	128 × 192, 2.2 × 1.47 mm, a slice 10 mm thick	–	57
1.5	^{1}H	agar gel doped with $CuSO_4$, human leg muscles	"	2D	256 × 256, (0.86 mm)^2, a slice 10 mm thick	60 or 69 s	58
1.5	^{1}H	agar gel	"	2D	256 × 256, (0.8 mm)^2, a slice 10 mm thick	1 min	59
1.5	^{1}H	water, acetone, oil	"	2D	256 × 128, 0.63 × 1.26 mm, a slice 5 mm thick	18 s	60
4.7	^{1}H	hind limb of a rat *in vivo*	FID	2D	32 × 32, (3 mm)^2, a slice 3 mm thick	2.5 min	61
3 (Ethylene glycol); 1.5 (liver)	^{1}H	ethylene glycol in a double cylinder; porcine liver *in vitro*	gradient echo (EPI)	2D	32 × 32; (6.45 mm)^2 (ethylene glycol); (5.16 mm)^2	10 s (ethylene glycol); 3 min (liver)	62
–	^{1}H	agar gel or porcine muscle and fat tissues	gradient echo	2D	256 × 256, (0.78 mm)^2	–	63
1.5	^{1}H	agar gel	the same	2D	256 × 256, (0.82 mm)^2, a slice 10 mm thick	26 s	64
1.5	^{1}H	1.5% agar gel doped with $CuSO_4$; turkey breast or pork	"	2D	256 × 256, (0.98 mm)^2, a slice 5 mm thick or 128 × 128, (1.2 mm)^2, a slice 10 mm thick	17 s	65
1.5	^{1}H	gel or porcine liver *ex vivo*	"	2D	128 × 128, (1.97 mm)^2	0.8 s	66
0.15	^{1}H	human peripheral muscle	"	–	–	–	67
1.5	^{1}H	silicone gel or rabbit femor *in vivo*	"	2D	96 × 128	7 – 20 s	68
0.2	^{1}H	agar gelatin or bull liver *ex vivo*	"	2D	128 × 128, (1.57 mm)^2, a slice 5 mm thick (gel); 256 × 256, (0.78 mm)^2, a slice 10 mm thick (liver)	4 s (gel); 13 s (liver)	69
1.5	^{1}H	water; gel; porcine brain and fat tissues *in vitro*; human brain	"	2D	180 × 256, 0.89 × 0.9 mm, a slice 4 – 5 mm thick	12 s	70
1.5	^{1}H	rabbit femor *in vivo*	gradient echo	2D	256 × 128, 0.63 × 1.26 mm, a slice 3 mm thick	3.3 s	72
4.7	^{1}H	agar gel	gradient echo (FLASH, PRESTO)	2D	64 × 60, (0.56 mm)^2, a slice 5 mm thick	144 ms (PRESTO)	73
1.89	^{31}P, ^{1}H	inorganic phosphate solutions in three coaxial cylinders or water in two ampoules	spin echo	2D	128 × 128	–	74
7, 11.7	^{1}H	DMSO, water or chloroform	FID	1D	170 μm	–	77
7, 11.7	^{1}H	convection in DMSO, water or chloroform	stimulated echo	–	WSR	–	77
0.15	^{1}H	human calf muscle	gradient echo	2D	128 × 128, (1.18 mm)^2, a slice 8 mm thick	–	80
1.5	^{1}H	sheep dug and fat tissues *in vivo*	the same	2D	256 × 256, (0.78 mm)^2, a slice 5 – 7 mm thick	2.3 s	81
4.7	^{1}H	agar gel	gradient echo (Snapshot FLASH)	2D	128 × 128, 0.4 × 0.8 mm, a slice 2 mm thick	2.1 s	82

Table S.1 (continued).

Field /T	Nucleus	Object, process	Technique	Dimension	Spatial resolution characteristics [a]	Recording time	Ref.
1.5	^{1}H	porcine muscle tissue, glandular tissue (sheep dug) or fat tissue	gradient echo (turboFLASH) with saturation – recovery	2D	256 × 256, $(0.94\ mm)^2$, a slice 10 mm thick	3 s	83
1.5	^{1}H	gel; bull muscles *in vitro* or rabbit muscles *in vivo*	gradient echo or spin echo	2D	192 × 256, 1.05 × 0.78 mm (gradient echo)	2 s (gradient echo), 112 s (spin echo)	84
1.5	^{1}H	gel or bull muscles *in vitro*	gradient echo	2D	$(1\ mm)^2$, a slice 5 mm thick	1.35 s	85
7.05	^{1}H	water + $CuSO_4$ in a tube or cylinder	spin echo	2D	256 × 128, $(0.27\ mm)^2$, a slice 2 mm thick or 1024 × 64, 0.078 × 0.23 mm, a slice 0.4 mm thick	17 min or 2 min	86
2	^{1}H	*cis*-polybutadiene block	gradient echo	2D	128 × 128, $(0.3\ mm)^2$, a slice 4 mm thick	–	87
1.5	^{1}H	polyacrylamide gel	–	2D	128 × 256, 1 × 2 mm, a slice 10 mm thick	3.5 min	88
1.5	^{1}H	agar gel doped with black ink and sodium aluminosilicate particles; or rabbit brain *in vivo*	gradient echo (EPI)	2D	128 × 256, 3 × 1.5 mm, a slice 6 mm thick	150 ms	89
0.5	^{1}H	human calf muscle	stimulated echo	1D	128, 1.97 mm, a slice 15 × 15 mm	51 s	90
1.5	^{1}H	bull muscles *in vitro*	gradient echo	2D	128 × 256, 1.9 × 0.9 mm, a slice 5 mm thick	1.8 or 5 s	91
7	^{1}H	CH_2Br_2 in a nematic liquid crystal	spin echo	1D	–	–	92
2.35	^{2}H	D_2O in a lyotropic liquid crystal	the same	–	WSR	–	94
0.5	^{1}H	porcine liver *in vivo* or *ex vivo*	gradient echo (GRASS)	2D	a slice 3 mm thick	1.2 – 3.5 min	95
2.35	^{1}H	rabbit liver *in vivo*	gradient echo	2D	256 × 192, 0.31 × 0.42 mm, a slice 4 mm thick	12 s	96
–	^{1}H	electric current flowing through coaxial cylinders filled with salt – water phantom and water; electric current flowing through a plant stem	spin echo	2D	$(60\ \mu m)^2$, a slice 2 or 3 mm thick	–	99
2	^{1}H	electric current flowing through coaxial cylinders filled with salt – water phantom	the same	2D	128 × 128; $(0.74\ mm)^2$, a slice 4 mm thick	–	100
2	^{1}H	electric current flowing through a ping-pong ball filled with salt – water phantom	"	2D	$(0.52\ mm)^2$	–	101
–	^{1}H	electric current flowing through coaxial cylinders filled with salt – water phantom; electric current flowing through a human forearm	"	2D	$(0.52\ mm)^2$, a slice 0.5 cm (cylinders) or 2 cm thick (forearm)	–	102
2.35	^{1}H	electric current flowing through a fragment of chicken femor soaked with salt – water phantom	"	2D	256 × 256; $(0.08\ mm)^2$, a slice 3 mm thick	18 min	103
4.7 (*in vivo*), 2.35 (*in vitro*)	^{1}H	electric current flowing through a mice tumour *in vivo* or *in vitro*	"	2D	256 × 256; $(0.12\ mm)^2$, a slice 2 mm thick	–	104
2.35	^{1}H	electric current flowing during NaCl dissolution in a water + agar mixture; electric current flowing through a water + $Ca(OH)_2 + CO_2$ mixture	"	2D	256 × 256; $(0.08\ mm)^2$, a slice 3 mm thick	–	105
2	^{1}H	electric current flowing through coaxial cylinders filled with salt – water phantom	"	2D	128 × 128; $(0.55\ mm)^2$	–	106

Table S.1 (continued).

Field /T	Nucleus	Object, process	Technique	Dimension	Spatial resolution characteristics [a]	Recording time	Ref.
–	^{1}H	electric current flowing through coaxial cylinders filled with salt – water phantom and water	spin echo	2D	128 × 128; (0.55 mm)^2	–	107
2	^{1}H	electric current flowing through coaxial cylinders filled with doped water or mineral oil, electric current flowing through a rat body *ex vivo*	the same	2D	128 × 128; (0.55 mm)^2, a slice 5 mm thick (cylinders); 128 × 128; (0.8 mm)^2, a slice 5 mm thick (rat)	–	108
2.35	^{1}H	electric current flowing through a rat brain *in vivo*	"	2D	256 × 256; (0.27 mm)^2, a slice 2 mm thick	–	109
2.35	^{1}H	rat brain *in vivo*	RF-CDI + spin echo	2D	256 × 256, (275 μm)^2, a slice 2 mm thick	–	109
3	^{1}H	electric current flowing through a copper conductor 60 μm in diameter placed in $H_2O + NaCl + CuSO_4$ phantom solution	gradient echo	2D	256 × 256, (0.47 mm)^2 or 64 × 64, (1.9 mm)^2, a slice 7 mm thick	–	110
3	^{1}H	a copper conductor in an aqueous solution containing 0.75% NaCl + 5 mM $CuSO_4$	gradient echo (EPI)	2D	64 × 64, (1.9 mm)^2, a slice 7 mm thick	–	110
1.4	^{1}H	electric current flowing through a LiCl + H_2O or $(CH_3)_4NCl$ + D_2O solution	spin echo	–	WSR	–	111
2.4	^{1}H	CH_4 in a cylinder with partitions	SPRITE	1D	128 points, 700 μm	–	112
2.4	^{19}F	SF_6 in a porous coral	SPRITE	3D	64 × 64 × 64, 2.5 mm	1.5 h	112
1.9	^{19}F	a $SF_6 - O_2$ (80 : 20 or 25 : 75) mixture in rat lungs	FID, PRI	3D	72 × 74 × 80, 529 μm	30.3 min	113
1.9	^{19}F	a $C_2F_6 - O_2$ (80 : 20) mixture in rat lungs	PRI	3D	46 × 46 × 54, 700 μm	4.3 h	114
7	^{19}F	C_2F_6 (5 atm) in a ceramic composite	spin echo	2D	(100 μm)^2, a slice 0.5 mm thick	12 h	115
1.9	^{19}F	C_2F_6 or C_4F_8 in ceramics (Y-stabilised zirconia)	the same	3D	–	2 h	116
9.4	^{129}Xe*	xenon in NaY and CaA zeolites and in porous glass	FID	2D	128 × 128, (156 μm)^2, a slice 4 mm thick	30 min	117
1.5	^{3}He*	helium in human lungs	gradient echo	2D	256 × 128, 2.1 × 4.1 mm, a slice 9 mm thick	20 s (a total of 8 slices)	119
2.35	^{3}He*	^{3}He (0.5 atm) in a glass cell	gradient echo (FLASH)	2D	32 × 64, 2.2 × 1.1 mm, a slice 2 cm thick	6.4 s	120
1.5	^{3}He*, ^{3}He	^{3}He* (1 atm) or a ^{3}He – O_2 mixture (73 : 27, 3.6 atm) in a glass cell	gradient echo	2D	96 × 128, 5.2 × 3.9 mm, a slice 40 mm thick (^{3}He*), 64 × 64, (4.7 mm)^2, a slice 40 mm thick	13 – 20 s (^{3}He*)	121
–	^{129}Xe*	gaseous Xe and Xe dissolved in perfluorinated solvent	the same	2D	–	–	122
9.4	^{129}Xe	Xe (30 atm) with O_2 additive in aerogel	chemical shift selective spin echo imaging	3D	(420 μm)^2, a slice 1 mm thick	–	123
1.5	^{129}Xe	Xe (0.78 atm) + O_2 (0.15 atm) in a glass sphere	FID after selective inversion	1D	1024 points, 0.5 mm (2 mm)		124
9.4	^{129}Xe*	xenon in porous glass	gradient echo	1D	–	–	127
2.35	^{129}Xe*	xenon in rat tissues *in vivo*	the same	2D	256 × 256, (1 mm)^2, a slice 10 mm thick	4.8 s	128
2, 7.05	^{129}Xe*	Xe + N_2 (10%) + Rb in a glass sphere at 790 or 896 Torr	FID	–	WSR	–	129
4.3	^{129}Xe*	Xe (1 – 3 atm, 80% ^{129}Xe) in nested tubes or in a capillary bunch	gradient echo (FLASH)	2D	128 × 64, 0.1 mm	–	130
4.3	^{129}Xe*	Xe (1 – 3 atm, 80% ^{129}Xe) in aerogel	the same	1D	0.1 mm	–	130

Table S.1 (continued).

Field /T	Nucleus	Object, process	Technique	Dimension	Spatial resolution characteristics [a]	Recording time	Ref.
4.2	^{129}Xe*	Xe (0.4 atm) + N_2 (0.27 atm) + He at a total pressure of 4 atm in capillaries and in a tube	gradient echo	2D	256 × 128, 110 × 340 μm, a slice 5 mm thick	51 min	131
4.2	^{129}Xe*	Xe (0.4 atm) + N_2 (0.27 atm) + He at a total pressure of 4 atm; flow through a tube with a diaphragm or through polyurethane foam	dynamic NMR microimaging (PGSE)	2D in the $k-q$ space	256 × 32, a slice 4 mm thick	–	131
4.3	^{129}Xe*	Xe (0.5 atm) + N_2 (0.5 atm) or Xe (3 atm) + N_2 (1 atm) in SiO_2 aerogel or in zeolite 13X	–	3D	250 × 250 × 100 μm (aerogel) 64 × 64 × 256, (100 μm)^3 (zeolite)	–	133
0.00206	^{3}He*	Rb + N_2 (100 Torr) + ^{3}He (2.7 atm) in a glass cell or in rat lungs *ex vivo*	gradient echo	2D	128 × 128, (1 mm)^2	25 s	134
0.0031	^{3}He*	Rb (10 – 100 mg) + N_2 (10 – 200 Torr) + ^{3}He (0.2 – 2.5 atm) in an ampoule with rectangular cross-section	FID	1D	–	–	135
1.5	^{3}He*	helium in human lungs	gradient echo (EPI)	2D	32 × 64, (6.25 mm)^2, a slice 10 mm thick	40.5 ms	136
0.0938	^{19}F	$CF_4 - O_2$ (80 : 20) mixture in dog lungs	PRI	3D	65 × 65 × 65, 0.5 – 1 cm	25 min	142
0.0938	^{19}F, ^{1}H	perfluorinated solution and water in two-compartmental phantom	PRI	3D	65 × 65 × 65, 2 – 3 mm	–	142
2.35	^{3}He, ^{1}H	helium in rat lungs	spin echo	2D	4.4 × 4.4 mm without slice selection (^{3}He), 128 × 64, 0.55 × 0.27 mm, a slice 5 mm thick (^{1}H)	8 min (^{3}He)	143
14.1	^{131}Xe	liquid Xe in aluminosilicate aerogel at 285 K	chemical shift selective spin echo imaging	3D	128 × 32 × 32, 0.47 × 0.38 × 0.38 mm	3 h	147
11.75	^{129}Xe*	Xe + He in tris(*o*-phenylenedioxy)-cyclophosphazene crystallites	broad-line NMR	–	WSR	–	148
1.9	^{3}He*	^{3}He (7 atm) in a cylinder	gradient echo	1D	0.8 mm	–	149
4.3	^{129}Xe*, ^{1}H*	xenon (80% ^{129}Xe) at 1 atm dissolved in C_6H_6 or $C_6D_6 - C_6D_5H$ (3 : 1) mixture	gradient echo (FLASH)	2D (^{129}Xe), EPI 2D (^{1}H)	128 × 64 (^{129}Xe), 128 × 32 (^{1}H)	24 ms (^{1}H)	150
4.2	^{129}Xe*	xenon in aerosil (or in modified aerosil), in CsI or in their mixture	–	–	WSR	–	151
2.0	^{3}He*	helium in guinea pig lungs *ex vivo*	gradient echo (GRASS)	2D, 3D	128 × 256, 0.56 × 0.28 mm, a slice 10 mm thick (2D); 128 × 256 × 32, 0.48 × 0.24 × 0.5 mm (3D)	1.41 s (2D)	157
2.0	^{3}He*	helium in guinea pig lungs *in vivo*	PRI	2D, 3D	(400 μm)^2 (2D)	–	158
2.0	^{3}He*	the same	PRI	2D, 3D	128 × 128 × 128, (0.5 mm)^3	6.4 min (3D)	159
2.0	^{3}He*	"	FID, radial trajectories	2D	256 × 256, (188 μm)^2	24 s	160
1.5	^{3}He*	helium in human lungs	the same	2D	256 × 256, (1.3 mm)^2		160
2.0	^{3}He*	helium in guinea pig lungs *in vivo*	"	2D	512 × 512, (102 μm)^2	100 s	161
2.0	^{3}He*	helium in rat lungs *in vivo*	PRI	2D, 3D	128 × 128 × 128, (550 μm)^3	54 s	162
0.79	^{3}He*, ^{1}H	helium in human lungs	gradient echo (FLASH)	2D	256 × 256, (1.2 mm)^2, a slice 3 mm thick	28 s	163
0.8	^{3}He*	helium in glass cells	the same	2D, 3D	256 × 256 × 32, 1 × 1 × 3 mm (3D)	3 min	164
0.8	^{3}He*, ^{1}H	helium in human lungs or upper respiratory tract	"	2D	1 – 2 mm in-plane resolution, a slice 30 mm thick	14 – 28 s	164

Table S.1 (continued).

Field /T	Nucleus	Object, process	Technique	Dimension	Spatial resolution characteristics [a]	Recording time	Ref.
1.5	^{3}He*, ^{1}H	helium in human lungs	gradient echo	2D	128 × 256, 1.25 × 2.5 mm, a slice 20 or 6 mm thick	0.9 s	166
1.5	^{3}He*, ^{1}H	helium in human paranasal sinuses	the same	2D	256 × 128, 0.9 × 1.9 mm, a slice 20 mm thick (He)	< 5 s (for 2 slices, He)	167
1.5	^{3}He*	helium in human lungs	gradient echo (FLASH)	3D	144 × 256 × 24, 2.4 × 1.4 × 7 mm	35 s	168
1.5	^{3}He*	the same	the same	3D	144 × 256 × 24, 2.4 × 1.4 × 7 mm	42 s	169
2.0	^{3}He*	helium in guinea pig lungs *in vivo* *in vivo*	PRI	2D	512 × 512, (73 μm)^2, a slice 16 mm thick	8 min	170
2.0	^{3}He*, ^{129}Xe*	helium or Xe (82% ^{129}Xe) in guinea pig lungs *in vivo*	FID, radial trajectories	2D	256 × 256, (190 μm)^2, a slice 5 mm thick (^{3}He); 128 × 128, (845 μm)^2 (^{129}Xe)	30 s	171
2.0	^{3}He*, ^{129}Xe*	the same	the same	2D	256 × 256, (190 μm)^2, a slice 5 mm thick (^{3}He); 128 × 128, (840 μm)^2 (^{129}Xe)	60 s	172
1.5	^{3}He*	helium in human lungs	"	2D	256 × 256, (1.41 mm)^2	16 s	172
1.5	^{3}He*	helium in a silicon bag or in porcine lungs (*in vivo* or *ex vivo*) or in human lungs	gradient echo	2D	81 × 128, 4 × 2.5 mm, a slice 180 mm (*Homo sapiens*) or 120 mm thick	0.9 s	173
9.4	^{129}Xe*	Xe (10^{19} cm^{-3}, 70% ^{129}Xe) in mice lungs *in vitro*	gradient echo (FLASH)	2D	128 × 128, (0.37 mm)^2	600 ms	174
9.4	^{129}Xe*	xenon (70% ^{129}Xe) in mice lungs *in vivo*	the same	2D	64 × 64, (0.39 mm)^2, a slice 2 mm	250 ms	175
4.7	^{129}Xe*	xenon in rat lungs *in vivo*	"	2D	2.3 × 4.7 mm, a slice 15 mm thick	1.3 s	176
1.5	^{129}Xe*	xenon (71% ^{129}Xe) in human lungs	"	2D	64 × 128, (6.6 mm)^2, a slice 20 mm thick	12 s	177
1.5	^{129}Xe*	xenon in the human oral cavity	gradient echo	2D	256 × 128, 1.6 × 3.1 mm, a slice 1 cm thick	–	178
2.0	^{3}He*, ^{129}Xe*	helium or Xe in guinea pig lungs *in vivo*	FID, radial trajectories	2D	256 × 256, (188 μm)^2 (^{3}He), 128 × 128, (847 μm)^2 (^{129}Xe)	4 s (^{3}He), 8 s (^{129}Xe)	179
2.0	^{3}He*, ^{129}Xe*	helium or Xe (82% ^{129}Xe) in guinea pig lungs *in vivo*	the same	3D	128 × 32 × 128; 0.37 × 1.2 × 0.37 mm (^{3}He), 0.56 × 1.25 × 0.56 mm (^{129}Xe)	–	180
2.0	^{129}Xe*, ^{1}H	xenon in rat lungs, blood and tissues *in vivo*	phase encoding, FID	1D, 2D	64 points, 1.8 mm (1D); 32 × 32, (1.9 mm)^2 or (3.1 mm)^2 (2D)	4 min (2D)	181
2.0	^{129}Xe*, ^{1}H	xenon in rat brain *in vivo*	chemical shift selective imaging	2D	32 × 32, (1.6 mm)^2, a slice 10 mm thick (Xe)	73 s	184
4.2	^{129}Xe*	xenon (80% ^{129}Xe) in human blood *in vitro*	spin echo (EPI)	2D	128 × 64	–	185
2.0	^{129}Xe*	xenon (82% ^{129}Xe) in rat blood *in vivo*	gradient echo (GRASS)	–	256 × 256 (256 × 128)	10 s	186
2.0	^{3}He*, ^{1}H	xenon (80% ^{129}Xe) in rat blood *in vivo*	gradient echo (time-of-flight angiography for ^{1}H)	2D	256 × 256, (0.31 mm)^2 (a slice 0.7 mm thick for ^{1}H)	–	187
4.7	^{1}H	vulcanised rubber impregnated with aluminium and sodium sulfate crystals, filled phenolaldehyde resin, or a 72-h *Manduca sexta* caterpillar	spin echo or PRI	–	180 FID, (35 μm)^2 (PRI); 128 × 128, a slice 1 mm thick or without slice selection	2 – 17 h	192
0.5	^{19}F	a fluoroplastic cylinder	PRI	2D	1 mm	–	194
9.4	^{1}H	hexamethylbenzene powder	magic echo	3D	64 × 64 × 64; (300 μm)^3	70 h	197

Table S.1 (continued).

Field /T	Nucleus	Object, process	Technique	Dimension	Spatial resolution characteristics [a]	Recording time	Ref.
2.35	^{1}H	agar gel doped with Mn(II), mortar, concrete or polyethylene	SPRITE	2D	64×64, $(1.25\ \text{mm})^2$ – $(1.5\ \text{mm})^2$	–	206
0.73	^{1}H	plastic or rubber items	gradient echo with oscillating gradients	3D	$64 \times 64 \times 64$; $(0.5\ \text{mm})^3$	3 h 38 min	209
0.4	^{1}H	various solid materials	spin echo	–	WSR	–	228
–	^{1}H	a glass supported tripropylene glycol diacrylate film, butadiene–styrene rubber	magic echo or gradient echo	1D	350 μm	–	235
4.7	^{1}H, ^{13}C	$CHCl_3$ or 0.3 M $CHCl_3$ in $CDCl_3$ in an ampoule or between two coaxial cylinders	spin echo	1D	–	–	270
1.4	^{1}H	water or agar gel in a tube	the same	–	WSR	–	271
7	^{1}H	water in coaxial tubes	spin echo or stimulated echo	2D	64×64; $(50\ \mu\text{m})^2$, a slice 1.2 mm thick	–	272
9.4	^{1}H	water or polydimethylsiloxane in a packed bead of silica granules	spin echo	–	WSR	–	273
1.5	^{1}H	rabbit skeletal muscle or kidney cortex (*in vivo*)	gradient echo	2D	256×128, 0.63×1.26 mm, a slice 5 mm thick	7–18 s	274
1.5	^{1}H	polyacrylamide gel or porcine liver *in vitro*	gradient echo or spin echo	2D	256×192, 0.78×1.05 mm, a slice 5 mm thick	–	275

Note: PRI is projection reconstructed imaging, WSR is without spatial resolution, FID is free induction decay, EPI is echo-phanar imaging and FLASH is fast low-angle shot.

[a] Listed are the image dimension (in pixels), spatial resolution and slice thickness.

References

1. I V Koptyug, R Z Sagdeev *Usp. Khim.* **71** 672 (2002) [*Russ. Chem. Rev.* **71** 593 (2002)]
2. I V Koptyug, R Z Sagdeev *Usp. Khim.* **71** 899 (2002) [*Russ. Chem. Rev.* **71** 789 (2002)]
3. R J Field, M Burger (Eds) *Oscillation and Travelling Waves in Chemical Systems* (New York: Wiley, 1985)
4. T A Carpenter, L D Hall, P Jezzard, C J Wiggins, N J Clayden, P Jackson, N Walton, in *Magnetic Resonance Microscopy. Methods and Applications in Materials Science, Agriculture and Biomedicine* (Eds B Blümich, W Kuhn) (Weinheim: VCH, 1992) p. 267
5. P Jackson, N J Clayden, N J Walton, T A Carpenter, L D Hall, P Jezzard *Polym. Int.* **24** 139 (1991)
6. A Yamazaki, Y Hotta, H Kurosu, I Ando *J. Mol. Struct.* **554** 47 (2000)
7. S Ahuja, S L Dieckman, N Gopalsami, A C Raptis *Macromolecules* **29** 5356 (1996)
8. P Jackson *J. Mater. Sci.* **27** 1302 (1992)
9. A Mavrich, F Fondeur, H Ishida, J L Koenig, H D Wagner *J. Adhes.* **46** 91 (1994)
10. P Blumler, B Blumich *Rubber Chem. Technol.* **70** 468 (1997)
11. C Fulber, K Unseld, V Herrmenn, K H Jakob, B Blumich *Colloid Polym. Sci.* **274** 191 (1996)
12. B J Balcom, T A Carpenter, L D Hall *Macromolecules* **25** 6818 (1992)
13. T G Nunes, R Pires, J Perdigao, A Amorim, M Polido *Polymer* **42** 8051 (2001)
14. U Gunther, K Albert, M Grossa *J. Magn. Reson.* **98** 593 (1992)
15. K Albert, U Gunther, M Ilg, E Bayer, M Grossa, in *Magnetic Resonance Microscopy. Methods and Applications in Materials Science, Agriculture and Biomedicine*. (Eds B Blümich, W Kuhn) (Weinheim: VCH, 1992) p. 277
16. A Ertl, A Berg, M Zehetmayer, P Frigo *Magn. Reson. Imaging* **18** 343 (2000)
17. B J Balcom, T J Lees, A R Sharp, N S Kulkarni, G S Wagner *Phys. Med. Biol.* **40** 1665 (1995)
18. F de Pasquale, G Sebastiani, E Egger, L Guidoni, A M Luciani, P Marzola, R Manfredi, M Pacilio, A Piermattei, V Viti, P Barone *Magn. Reson. Imaging* **18** 721 (2000)
19. M McJury, M Oldham, O M Leach, S Webb *Phys. Med. Biol.* **44** 1863 (1999)
20. P Haraldsson, S A J Back, P Magnusson, L E Olsson *Br. J. Radiol.* **73** 58 (2000)
21. E Pappas, I Seimenis, A Angelopoulos, P Georgolopoulou, M Kamariotaki-Paparigopoulou, T Maris, L Sakelliou, P Sandilos, L Vlachos *Phys. Med. Biol.* **46** 783 (2001)
22. E W Hansen, P Ruoff *J. Phys. Chem.* **93** 264 (1989)
23. A R Cross, R L Armstrong, A Reid, S Su, M Menzinger *J. Phys. Chem.* **99** 16 616 (1995)
24. A Tzalmona, R L Armstrong, M Menzinger, A Cross, C Lemaire *Chem. Phys. Lett.* **174** 199 (1990)
25. A L Cross, R L Armstrong, C Gobrecht, M Paton, C Ware *Magn. Reson. Imaging* **15** 719 (1997)
26. A Tzalmona, R L Armstrong, M Menzinger, A Cross, C Lemaire *Chem. Phys. Lett.* **188** 457 (1992)
27. M Menzinger, A Tzalmona, R L Armstrong, A Cross, C Lemaire *J. Phys. Chem.* **96** 4725 (1992)
28. S Su, R L Armstrong, M Menzinger, A Cross, C Lemaire *J. Chem. Phys.* **98** 7295 (1993)
29. R L Armstrong, A Tzalmona, M Menzinger, A Cross, C Lemaire, in *Magnetic Resonance Microscopy. Methods and Applications in Materials Science, Agriculture and Biomedicine*. (Eds B Blümich, W Kuhn) (Weinheim: VCH, 1992) p. 309
30. S Su, M Menzinger, R L Armstrong, A Cross, C Lemaire *J. Phys. Chem.* **98** 2494 (1994)
31. Y Gao, A R Cross, R L Armstrong *J. Phys. Chem.* **100** 10159 (1996)
32. B J Balcom, A Carpenter, L D Hall *J. Chem. Soc., Chem. Commun.* 312 (1992)
33. B J Balcom, T A Carpenter, L D Hall *Can. J. Chem.* **70** 2693 (1992)

34. K Potter, B J Balcom, T A Carpenter, L D Hall *Carbohydr. Res.* **257** 117 (1994)
35. J J Tessier, T A Carpenter, L D Hall *J. Magn. Reson., Ser. A* **113** 232 (1995)
36. L G Butler, D G Cory, K M Dooley, J B Miller, A N Garroway *J. Am. Chem. Soc.* **114** 125 (1992)
37. K M Salikhov, Yu N Molin, R Z Sagdeev, A L Buchachenko *Spin Polarization and Magnetic Effects in Radical Reactions* (Budapest: Akademiai Kiado, 1984)
38. A L Buchachenko, R Z Sagdeev, K M Salikhov *Magnitnye i Spinovye Effekty v Khimicheskikh Reaktsiyakh* (Magnetic and Spin Effects in Chemical Reactions) (Novosibirsk: Nauka, 1978)
39. A A Obynochny, A G Maryasov, K A Ilyasov, O I Gnezdilov, K M Salikhov *Appl. Magn. Reson.* **17** 609 (1999)
40. C R Bowers, D P Weitekamp *J. Am. Chem. Soc.* **109** 5541 (1987)
41. S B Duckett, C J Sleigh *Prog. Nucl. Magn. Reson. Spectrosc.* **34** 71 (1999)
42. J Barkemeyer, M Haake, J Bargon *J. Am. Chem. Soc.* **117** 2927 (1995)
43. K Golman, O Axelsson, H Johannesson, S Mansson, C Olofsson, J S Petersson *Magn. Reson. Med.* **46** 1 (2001)
44. C Ammann, P Meier, A E Merbach *J. Magn. Reson.* **46** 319 (1982)
45. R D Peters, R S Hinks, R M Henkelman *Magn. Reson. Med.* **40** 454 (1998)
46. N J McDannold, R L King, F A Jolesz, K H Hynynen *Radiology* **216** 517 (2000)
47. J Kettenbach, S G Silverman, N Hata, K Kuroda, P Saiviroonporn, G P Zientara, P R Morrison, S G Hushek, P M Black, R Kikins, F A Jolesz *J. Magn. Reson. Imaging* **8** 933 (1998)
48. V U Fiedler, H-J Schwarzmaier, F Eickmeyer, F P Muller, C Schoepp, P R Verreet *J. Magn. Reson. Imaging* **13** 729 (2001)
49. W Wlodarczyk, R Boroschewski, M Henyschel, P Wust, G Monich, R Felix *J. Magn. Reson. Imaging* **8** 165 (1998)
50. H P Shukla, R P Mason, D E Woessner, P P Antich *J. Magn. Reson., Ser. B* **106** 131 (1995)
51. G C Levy, J T Bailey, D A Wright *J. Magn. Reson.* **37** 353 (1980)
52. Y Ishihara, A Calderon, H Watanabe, K Okamoto, Y Suzuki, K Kuroda, Y Suzuki *Magn. Reson. Med.* **34** 814 (1995)
53. K P Nott, L D Hall, J R Bows, M Hale, M L Patrick *Magn. Reson. Imaging* **18** 69 (2000)
54. T Kahn, T H Harth, J C W Kiwit, H-J Schwarzmaier, C Wald, U Modder *J. Magn. Reson. Imaging* **8** 160 (1998)
55. J A Moriarty, J C Chen, C M Purcell, L C Ang, R S Hinks, R D Peters, R M Henkelman, D B Plewes, M J Bronskill, W Kucharczyk *J. Magn. Reson. Imaging* **8** 128 (1998)
56. T Harth, T Kahn, M Rassek, B Schwabe, H-J Schwarzmaier, J S Lewin, U Modder *Magn. Reson. Med.* **38** 238 (1997)
57. I R Young, J V Hajnal, I G Roberts, J X Ling, R J Hill-Cottingham, A Oatridge, J A Wilson *Magn. Reson. Med.* **36** 366 (1996)
58. J De Poorter, C De Wagter, Y De Deene, C Thomsen, F Stahlberg, E Achten *Magn. Reson. Med.* **33** 74 (1995)
59. J De Poorter, C De Wagter, Y De Deene, C Thomsen, F Stahlberg, E Achten *J. Magn. Reson., Ser. B* **103** 234 (1994)
60. K Kuroda, K Oshio, A H Chung, K Hynynen, F A Jolesz *Magn. Reson. Med.* **38** 845 (1997)
61. K Kuroda, Y Suzuki, Y Ishihara, K Okamoto, Y Suzuki *Magn. Reson. Med.* **35** 20 (1996)
62. K Kuroda, R V Mulkern, K Oshio, L P Panych, T Nakai, T Moriya, S Okuda, K Hynynen, F A Joles *Magn. Reson. Med.* **43** 220 (2000)
63. J De Poorter *Magn. Reson. Med.* **34** 359 (1995)
64. R D Peters, R S Hinks, R M Henkelman *Magn. Reson. Med.* **41** 909 (1999)
65. F Bertsch, J Mattner, M K Stehling, U Muller-Lisse, M Peller, R Loeffler, J Weber, K Messmer, W Wilmanns, R Issels, M Reiser *Magn. Reson. Imaging* **16** 393 (1998)
66. J Heisterkamp, N A A Matheijssen, R van Hillegersberg, J J van Vaals, J S Lameris, J Stoker, J N M I Jzermans *Magn. Reson. Med.* **41** 919 (1999)
67. I R Young, J W Hand, A Oatridge, M V Prior *Magn. Reson. Med.* **32** 358 (1994)
68. R V Mulkern, L P Panych, N J McDannold, F A Jolesz, K Hynynen *J. Magn. Reson. Imaging* **8** 493 (1998)
69. S Sinha, T Oshiro, U Sinha, R Lufkin *J. Magn. Reson. Imaging* **7** 918 (1997)
70. R Stollberger, P W Ascher, D Huber, W Renhart, H Radner, F Ebner *J. Magn. Reson. Imaging* **8** 188 (1998)
71. T J Vogl, M G Mack, P Muller, C Phillip, H Bottcher, A Roggan, M Juergens, M Deimling, D Knobber, P Wust *Radiology* **196** 725 (1995)
72. K Kuroda, A H Chung, K Hynynen, F A Jolesz *J. Magn. Reson. Imaging* **8** 175 (1998)
73. J A de Zwart, P van Gelderen, D J Kelly, C T W Moonen *J. Magn. Reson., Ser. B* **112** 86 (1996)
74. L D Hall, S L Talagala *J. Magn. Reson.* **65** 501 (1985)
75. C S Zuo, J L Bowers, K R Metz, T Nosaka, A D Sherry, M E Clouse *Magn. Reson. Med.* **36** 955 (1996)
76. C S Zuo, K R Metz, Y Sun, A D Sherry *J. Magn. Reson.* **133** 53 (1998)
77. N M Loening, J Keeler *J. Magn. Reson.* **139** 334 (1999)
78. T Frenzel, K Roth, S Kossler, B Raduchel, H Bauer, J Platzek, H-J Weinmann *Magn. Reson. Med.* **35** 364 (1996)
79. S Aime, M Botta, M Fasano, E Terreno, P Kinchesh, L Calabi, L Paleari *Magn. Reson. Med.* **35** 648 (1996)
80. I R Young, J W Hand, A Oatridge, M V Prior, G R Forse *Magn. Reson. Med.* **31** 342 (1994)
81. C Bohris, J W Jenne, R Rastert, I Simiantonakis, G Brix, J Spoo, M Hlavac, R Nemeth, P E Huber, J Debus *Magn. Reson. Imaging* **19** 167 (2001)
82. C Schwarzbauer, J Zange, H Adolf, R Deichmann, U Noth, A Haase *J. Magn. Reson., Ser. B* **106** 178 (1995)
83. C Bohris, W G Schreiber, J Jenne, I Simiantonakis, R Rastert, H-J Zabel, P Huber, R Bader, G Brix *Magn. Reson. Imaging* **17** 603 (1999)
84. H E Cline, J F Schenk, R D Watkins, K Hynynen, F A Jolesz *Magn. Reson. Med.* **30** 98 (1993)
85. H E Cline, K Hynynen, C J Hardy, R D Watkins, J F Schenck, F A Jolesz *Magn. Reson. Med.* **31** 628 (1994)
86. K Ogawa, M Tobo, N Iriguchi, S Hirai, K Okazaki *Magn. Reson. Imaging* **18** 209 (2000)
87. S J Doran, T A Carpenter, L D Hall *Rev. Sci. Instrum.* **65** 2231 (1994)
88. J Delannoy, C-N Chen, R Turner, R L Levin, D Le Bihan *Magn. Reson. Med.* **19** 333 (1991)
89. A R Bleier, F A Jolesz, M S Cohen, R M Weisskoff, J J Dalcanton, N Higuchi, D A Feinberg, B R Rosen, R C McKinstry, S G Hushek *Magn. Reson. Med.* **21** 132 (1991)
90. D Morvan, A Leroy-Willig, A Malgouyres, C A Cuenod, P Jehenson, A Syrota *Magn. Reson. Med.* **29** 371 (1993)
91. H E Cline, K Hynynen, E Schneider, C J Hardy, S E Maier, R D Watkins, F A Jolesz *Magn. Reson. Med.* **35** 309 (1996)
92. N Hedin, I Furo *J. Magn. Reson.* **131** 126 (1998)
93. R D Farrant, J C Lindon *Magn. Reson. Chem.* **32** 231 (1994)
94. I Furo, H Johannesson *J. Magn. Reson., Ser. A* **119** 15 (1996)
95. E Samset, T Mala, B Edwin, I Gladhaug, O Soreide, E Fosse *Magn. Reson. Imaging* **19** 715 (2001)
96. J C Gilbert, B Rubinsky, S T S Wong, K M Breenan, G R Pease, P P Leung *Magn. Reson. Imaging* **15** 657 (1997)
97. N S Sullivan *Bull. Magn. Reson.* **18** 258 (1997)
98. B I Verkin (Ed.) *Metody Polucheniya i Izmereniya Nizkikh i Sverkhnizkikh Temperatur* (Methods of Creation and Measurement of Low and Ultra Low Temperatures) (Kiev: Naukova Dumka, 1987)
99. I Sersa, O Jarh, F Demsar *J. Magn. Reson., Ser. A* **111** 93 (1994)
100. G C Scott, M L G Joy, R L Armstrong, R M Henkelman *J. Magn. Reson.* **97** 235 (1992)
101. G C Scott, M L G Joy, R L Armstrong, R M Henkelman *IEEE Trans. Med. Imaging* **10** 362 (1991)
102. M Joy, G Scott, M Henkelman *Magn. Reson. Imaging* **7** 89 (1989)
103. K Beravs, D White, I Sersa, F Demsar *Magn. Reson. Imaging* **15** 909 (1997)
104. I Sersa, K Beravs, N J F Dodd, S Zhao, D Miklavcic, F Demsar *Magn. Reson. Med.* **37** 404 (1997)
105. K Beravs, A Demsar, F Demsar *J. Magn. Reson.* **137** 253 (1999)

106. G C Scott, M L G Joy, R L Armstrong, R M Henkelman *Magn. Reson. Med.* **28** 186 (1992)
107. G C Scott, M L G Joy, R L Armstrong, R M Henkelman *IEEE Trans. Med. Imaging* **14** 515 (1995)
108. G C Scott, M L G Joy, R L Armstrong, R M Henkelman *Magn. Reson. Med.* **33** 355 (1995)
109. K Beravs, R Frangez, A N Gerkis, F Demsar *Magn. Reson. Med.* **42** 136 (1999)
110. J Bodurka, A Jesmanowica, J S Hyde, H Xu, L Estkowski, S-J Li *J. Magn. Reson.* **137** 265 (1999)
111. M Holz, C Muller *J. Magn. Reson.* **40** 595 (1980)
112. P J Prado, B J Balcom, I V Mastikhin, A R Cross, R L Armstrong, A Logan *J. Magn. Reson.* **137** 324 (1999)
113. D O Kuethe, A Caprihan, H M Gach, I J Lowe, E Fukushima *J. Appl. Physiol.* **88** 2279 (2000)
114. D O Kuethe, A Caprihan, E Fukushima, R A Waggoner *Magn. Reson. Med.* **39** 85 (1998)
115. M J Lizak, M S Conradi, C G Fry *J. Magn. Reson.* **95** 548 (1991)
116. A Caprihan, C F M Clewett, D O Kuethe, E Fukushima, S J Glass *Magn. Reson. Imaging* **19** 311 (2001)
117. I L Moudrakovski, S Lang, C I Ratcliffe, B Simard, G Santyr, J A Ripmeester *J. Magn. Reson.* **144** 372 (2000)
118. W Happer, E Miron, S Schaefer, D Schreiber, W A van Wijngaarden, X Zeng *Phys. Rev., Sect. A* **29** 3092 (1984)
119. T R Gentile, G L Jones, A K Thompson, R R Rizi, D A Roberts, I E Dimitrov, R Reddy, D A Lipson, W Gefter, M D Schanll, J S Leigh *Magn. Reson. Med.* **43** 290 (2000)
120. F Kober, P-E Wolf, J-L Leviel, G Vermeulen, G Duhamel, A Delon, J Derouard, M Decorps, A Ziegler *Magn. Reson. Med.* **41** 1084 (1999)
121. M Bock *Magn. Reson. Med.* **38** 890 (1997)
122. J Wolber, I J Rowland, M O Leach, A Bifone *Appl. Magn. Reson.* **15** 343 (1998)
123. D M Gregory, R E Gerald II, R E Botto *J. Magn. Reson.* **131** 327 (1998)
124. M Pfeffer, O Lutz *J. Magn. Reson., Ser. A* **113** 108 (1995)
125. K L Sauer, R J Fitzgerald, W Happer *Chem. Phys. Lett.* **277** 153 (1997)
126. M Haake, B M Goodson, D D Laws, E Brunner, M C Cyrier, R H Havlin, A Pines *Chem. Phys. Lett.* **292** 686 (1998)
127. I L Moudrakovski, A Sanchez, C I Ratcliffe, J A Ripmeester *J. Phys. Chem. B* **104** 7306 (2000)
128. B M Goodson, Y-Q Song, R E Taylor, V D Schepkin, K M Brennan, G C Chingas, T F Budinger, G Navon, A Pines *Proc. Natl. Acad. Sci. USA* **94** 14725 (1997)
129. B R Patyal, J-H Gao, R F Williams, J Roby, B Saam, B A Rockwell, R J Thomas, D J Stolarski, P T Fox *J. Magn. Reson.* **126** 58 (1997)
130. Y-Q Song, H C Gaede, T Pietrass, G A Barrall, G C Chingas, G C Ayers, A Pines *J. Magn. Reson., Ser. A* **115** 127 (1995)
131. E Brunner, M Haake, L Kaiser, A Pines, J A Reimer *J. Magn. Reson.* **138** 155 (1999)
132. M Haake, A Pines, J A Reimer, R Seydoux *J. Am. Chem. Soc.* **119** 11711 (1997)
133. L G Kaiser, T Meersmann, J W Logan, A Pines *Proc. Natl. Acad. Sci. USA* **97** 2414 (2000)
134. G P Wong, C H Tseng, V R Pomeroy, R W Mair, D P Hinton, D Hoffmann, R E Stoner, F W Hersman, D G Cory, R L Walsworth *J. Magn. Reson.* **141** 217 (1999)
135. B Saam, N Drukker, W Happer *Chem. Phys. Lett.* **263** 481 (1996)
136. B Saam, D A Yablonsky, D S Gierada, M S Conradi *Magn. Reson. Med.* **42** 507 (1999)
137. M P Augustine, E L Hahn *J. Chem. Phys.* **107** 3324 (1997)
138. X Mao, J Chen *Chem. Phys.* **202** 357 (1996)
139. P Broekaert, J Jeener *J. Magn. Reson., Ser. A* **113** 60 (1995)
140. W E Maas, F H Laukien, D G Cory *J. Magn. Reson., Ser. A* **113** 274 (1995)
141. V L Berdinskii, A L Buchachenko, A D Pershin *Teor. Eksp. Khim.* **12** 666 (1976) [a]
142. P A Rinck, S B Petersen, P C Lauterbur *Fortschr. Roentgenstr.* **140** 239 (1984)
143. F Kober, B Koenigsberg, V Belle, M Viallon, J L Leviel, A Delon, A Ziegler, M Decorps *J. Magn. Reson.* **138** 308 (1999)
144. G C Chingas, J Milliken, H A Resing, T Tsang *Synth. Met.* **12** 131 (1985)
145. T Pietrass, J M Kneller, R A Assink, M T Anderson *J. Phys. Chem. B* **103** 8837 (1999)
146. N Bansal, C Dybowski *J. Magn. Reson.* **89** 21 (1990)
147. G Pavlovskaya, A K Blue, S J Gibbs, M Haake, F Cros, L Malier, T Meersmann *J. Magn. Reson.* **137** 258 (1999)
148. T Meersmann, J W Logan, R Simonutti, S Caldarelli, A Comotti, P Sozzani, L G Kaiser, A Pines *J. Phys. Chem. A* **104** 11665 (2000)
149. D M Schmidt, J S George, S I Penttila, A Caprihan, E Fukushima *J. Magn. Reson.* **129** 184 (1997)
150. G Navon, Y-Q Song, T Room, S Appelt, R E Taylor, A Pines *Science* **271** 1848 (1996)
151. R Seydoux, A Pines, M Haake, J A Reimer *J. Phys. Chem. B* **103** 4629 (1999)
152. H C Gaede, Y-Q Song, R E Taylor, E J Munson, J A Reimer, A Pines *Appl. Magn. Reson.* **8** 373 (1995)
153. E Brunner *Concepts Magn. Reson.* **11** 313 (1999)
154. J Smith, L J Smith, K Knagge, E MacNamara, D Raftery *J. Am. Chem. Soc.* **123** 2927 (2001)
155. B Driehuys, G D Cates, W Happer, H Mabuchi, B Saam, M S Albert, A Wishnia *Phys. Lett. A* **184** 88 (1993)
156. H W Long, H C Gaede, J Shore, L Reven, C R Bowers, J Kritzenberger, T Pietrass, A Pines, P Tang, J A Reimer *J. Am. Chem. Soc.* **115** 8491 (1993)
157. H Middleton, R D Black, B Saam, G D Cates, G P Cofer, R Guenther, W Happer, L W Hedlund, G A Johnson, K Juvan, J Swartz *Magn. Reson. Med.* **33** 271 (1995)
158. R D Black, H L Middleton, G D Cates, B Driehuys, W Happer, L W Hedlund, G A Johnson, M D Shattuck, J C Swartz *Radiology* **199** 867 (1996)
159. G A Johnson, G Cates, X J Chen, G P Cofer , B Driehuys, W Happer, L W Hedlund, B Saam, M D Shattuck, J Swartz *Magn. Reson. Med.* **38** 66 (1997)
160. X J Chen, M S Chawla, L W Hedlund, H E Moeller, J R MacFall, G A Johnson *Magn. Reson. Med.* **39** 79 (1998)
161. X J Chen, M S Chawla, G P Cofer, L W Hedlund, H E Moeller, G A Johnson *Magn. Reson. Med.* **40** 61 (1998)
162. Y Cremillieux, Y Berthezene, H Humbolt, M Viallon, E Canet, M Bourgeois, T Albert, W Heil, A Briguet *Magn. Reson. Med.* **41** 645 (1999)
163. M Ebert, T Grossmann, W Heil, W E Otten, R Surkau, M Leduc, P Bachert, M V Knopp, L R Schad, M Thelen *Lancet* **347** 1297 (1996)
164. P Bachert, L R Schad, M Bock, M V Knopp, M Ebert, T Grossmann, W Heil, D Hofmann, R Surkau, E W Otten *Magn. Reson. Med.* **36** 192 (1996)
165. M Leduc, E Otten *La Recherche* **287** 41 (1996)
166. J R MacFall, H C Charles, R D Black, H Middleton, J C Swartz, B Saam, B Driehuys, C Erickson, W Happer, G D Cates, G A Johnson, C E Ravin *Radiology* **200** 553 (1996)
167. R R Rizi, I E Dimitrov, A Thompson, G Jones, T R Gentile, M Ishii, R Reddy, M D Schnall, J S Leigh *Magn. Reson. Med.* **39** 865 (1998)
168. H-U Kauczor, M Ebert, K-F Kreitner, H Nilgens, R Surkau, W Heil, D Hofmann, E W Otten, M Thelen *J. Magn. Reson. Imaging* **7** 538 (1997)
169. H-U Kauczor, D Hofmann, K-F Kreitner, N Nilgens, R Surkau, W Heil, A Potthast, M V Knopp, E W Otten, M Thelen *Radiology* **201** 564 (1996)
170. M Viallon, G P Cofer, S A Suddarth, H E Moeller, X J Chen, M S Chawla, L W Hedlund, Y Cremillieux, G A Johnson *Magn. Reson. Med.* **41** 787 (1999)
171. X J Chen, H E Moeller, M S Chawla, G P Cofer, B Driehuys, L W Hedlund, G A Johnson *Magn. Reson. Med.* **42** 721 (1999)
172. X J Chen, H E Moeller, M S Chawla, G P Cofer, B Driehuys, L W Hedlund, J R MacFall, G A Johnson *Magn. Reson. Med.* **42** 729 (1999)

173. A J Deninger, B Eberle, M Ebert, T Grossmann, W Heil, H-U Kauczor, L Lauer, K Markstaller, E Otten, J Schmiedeskamp, W Schreiber, R Surkau, M Thelen, N Weiler *J. Magn. Reson.* **141** 207 (1999)
174. M S Albert, G D Cates, B Driehuys, W Happer, B Saam, C S Springer, A Wishnia *Nature (London)* **370** 199 (1994)
175. M E Wagshul, T E Button, H F Li, Z Liang, C S Springer, K Zhong, A Wishnia *Magn. Reson. Med.* **36** 183 (1996)
176. K Sakai, A M Bilek, E Oteiza, R L Walsworth, D Balamore, F A Jolesz, M S Albert *J. Magn. Reson., Ser. B* **111** 300 (1996)
177. J P Mugler III, B Driehuys, J R Brookeman, G D Cates, S S Berr, R G Bryant, T M Daniel, E E de Lange, J H Downs III, C J Erickson, W Happer, D P Hinton, N F Kassel, T Maier, C D Phillips, B T Saam, K L Sauer, M E Wagshul *Magn. Reson. Med.* **37** 809 (1997)
178. M S Albert, C H Tseng, D Williamson, E R Oteiza, R L Walsworth, B Kraft, D Kacher, B L Holman, F A Jolesz *J. Magn. Reson., Ser. B* **111** 204 (1996)
179. H E Moeller, X J Chen, M S Chawla, B Driehuys , L W Hedlund, G A Johnson *J. Magn. Reson.* **135** 133 (1998)
180. H E Moeller, X J Chen, M S Chawla, G P Cofer, B Driehuys, L W Hedlund, S A Suddarth, G A Johnson *Magn. Reson. Med.* **41** 800 (1999)
181. S D Swanson, M S Rosen, K P Coulter, R C Welsh, T E Chupp *Magn. Reson. Med.* **42** 1137 (1999)
182. M S Albert, D Balamore *Nucl. Instrum. Methods Phys. Res., Sect. A* **402** 441 (1998)
183. J Wolber, A Cherubini, A S K Dzik-Jurasz, M O Leach, A Bifone *Proc. Natl. Acad. Sci. USA* **96** 3664 (1999)
184. S D Swanson, M S Rosen, B W Agranoff, K P Coulter, R C Welsh, T E Chupp *Magn. Reson. Med.* **38** 695 (1997)
185. A Bifone, Y-Q Song, R Seydoux, R E Taylor, B M Goodson, T Pietrass, T F Budinger, G Navon, A Pines *Proc. Natl. Acad. Sci. USA* **93** 12932 (1996)
186. H E Moeller, M S Chawla, X J Chen, B Driehuys, L W Hedlund, C T Wheeler, G A Johnson *Magn. Reson. Med.* **41** 1058 (1999)
187. M S Chawla, X J Chen, H E Moller, G P Cofer, C T Wheeler, L W Hedlund, G A Johnson *Proc. Natl. Acad. Sci. USA* **95** 10832 (1998)
188. B Blümich, P Blümler, K Saito, in *Solid State NMR of Polymers. Studies in Physical and Theoretical Chemistry* Vol. 84 (Eds I Ando, T Asakura) (New York: Elsevier Science, 1998)
189. P Blumler, B Blumich *NMR Basic Princip. Prog.* **30** 209 (1994)
190. P Adriaensens, A Pollaris, D Vanderzande, J Gelan, J L White, M Kelchtermans *Macromolecules* **33** 7116 (2000)
191. P Adriaensens, A Pollaris, D Vanderzande, J Gelan, J L White, A J Dias, M Kelchtermans *Macromolecules* **32** 4692 (1999)
192. J M Listerud, S W Sinton, G P Drobny *Anal. Chem.* **61** 23A (1989)
193. J B Miller, D G Cory, A N Garroway *Philos. Trans. R. Soc. London, Ser. A* **333** 413 (1990)
194. F De Luca, B C De Simone, N Lugeri, B Maraviglia *J. Magn. Reson., Ser. A* **102** 287 (1993)
195. D G Cory *Annu. Rep. Nucl. Magn. Reson.* **24** 87 (1992)
196. D G Cory, J B Miller, A N Garroway *J. Magn. Reson.* **90** 205 (1990)
197. S Hafner, P Barth, W Kuhn *J. Magn. Reson., Ser. A* **108** 21 (1994)
198. S Matsui *Chem. Phys. Lett.* **179** 187 (1991)
199. S Choi, X-W Tang, D G Cory *Int. J. Imaging Syst. Technol.* **8** 263 (1997)
200. S Gravina, D G Cory *J. Magn. Reson., Ser. B* **104** 53 (1994)
201. S D Beyea, B J Balcom, I V Mastikhin, T W Bremner, R L Armstrong, P E Grattan-Bellew *J. Magn. Reson.* **144** 255 (2000)
202. B J Balcom, R P MacGregor, S D Beyea, D P Green, R L Armstrong, T W Bremner *J. Magn. Reson., Ser. A* **123** 131 (1996)
203. B J Balcom, in *Spatially Resolved Magnetic Resonance. Methods, Materials, Medicine, Biology, Rheology, Geology, Ecology, Hardware* (Eds B Blümich P.Blümler R.Botto E.Fukushima) (Weinheim: Wiley-VCH, 1998) p. 75
204. I V Mastikhin, B J Balcom, P J Prado, C B Kennedy *J. Magn. Reson.* **136** 159 (1999)
205. C B Kennedy, B J Balcom, I V Mastikhin *Can. J. Chem.* **76** 1753 (1998)
206. S D Beyea, B J Balcom, P J Prado, A R Cross, C B Kennedy, R L Armstrong, T W Bremner *J. Magn. Reson.* **135** 156 (1998)
207. G R Davies, D J Lurie, J M S Hutchison, S J McCallum, I Nicholson *J. Magn. Reson.* **148** 289 (2001)
208. W Zhang, D G Cory *J. Magn. Reson.* **132** 144 (1998)
209. M J D Mallett, S L Codd, M R Halse, T A P Green, J H Strange *J. Magn. Reson., Ser. A* **119** 105 (1996)
210. J H Strange *Philos. Trans. R. Soc. London, Ser. A* **333** 427 (1990)
211. M J D Mallett, J H Strange *Appl. Magn. Reson.* **12** 193 (1997)
212. S L Codd, M J D Mallett, M R Halse, J H Strange, W Vennart, T Van Doorn *J. Magn. Reson., Ser. B* **113** 214 (1996)
213. A A Samoilenko, D Yu Artemov, L A Sibeldina *Bruker Rep.* **2** 30 (1987)
214. A A Samoilenko, D Yu Artemov, L A Sibeldina *JETP Lett.* **47** 417 (1988)
215. P J McDonald *Prog. Nucl. Magn. Reson. Spectrosc.* **30** 69 (1997)
216. P Kinchesh, E W Randall, K Zick *J. Magn. Reson.* **100** 411 (1992)
217. T B Benson, P J McDonald *J. Magn. Reson., Ser. B* **109** 314 (1995)
218. E W Randall, A A Samoilenko, T Nunes *J. Magn. Reson., Ser. A* **116** 122 (1995)
219. M J D Mallett, M R Halse, J H Strange *J. Magn. Reson.* **132** 172 (1998)
220. R R Ernst, G Bodenhausen, A Wokaun *Principles of Nuclear Magnetic Resonance in One and Two Dimensions* (Oxford: Clarendon Press, 1987)
221. A N Garroway, J Baum, M G Munowitz, A Pines *J. Magn. Reson.* **60** 337 (1984)
222. D E Demco, S Hafner, R Kimmich *Appl. Magn. Reson.* **9** 267 (1995)
223. D E Demco, S Hafner, I Ardeleanu, R Kimmich *Appl. Magn. Reson.* **9** 491 (1995)
224. M Corti, F Borsa, A Rigamonti *J. Magn. Reson.* **79** 21 (1988)
225. A Spyros, N Chandrakumar, M Heidenreich, R Kimmich *Macromolecules* **31** 3021 (1998)
226. J J H Ackerman *Concepts Magn. Reson.* **2** 33 (1990)
227. B Blumich, P Blumler, G Eidmann, A Guthausen, R Haken, U Schmitz, K Saito, G Zimmer *Magn. Reson. Imaging* **16** 479 (1998)
228. G Eidmann, R Savelsberg, P Blumler, B Blumich *J. Magn. Reson., Ser. A* **122** 104 (1996)
229. P J Prado, B Blumich, U Schmitz *J. Magn. Reson.* **144** 200 (2000)
230. B Blumich *Concepts Magn. Reson.* **10** 19 (1998)
231. B Blumich *Concepts Magn. Reson.* **11** 71 (1999)
232. B Blumich *Concepts Magn. Reson.* **11** 147 (1999)
233. P Barth, S Hafner, P Denner *Macromolecules* **29** 1655 (1996)
234. A Guthausen, G Zimmer, P Blumler, B Blumich *J. Magn. Reson.* **130** 1 (1998)
235. D E Demco, F Weigand, C Fulber, X Filip, C Filip *Appl. Magn. Reson.* **12** 363 (1997)
236. L Gasper, D E Demco, B Blumich *Solid State Nucl. Magn. Reson.* **14** 105 (1999)
237. M Schneider, D E Decmo, B Blumich *Macromolecules* **34** 4019 (2001)
238. M A Hepp, J B Miller *J. Magn. Reson., Ser. A* **111** 62 (1994)
239. P Barth, S Hafner *Magn. Reson. Imaging* **15** 107 (1997)
240. M Knorgen, U Heuert, H Menge, H Schneider *Angew. Makromol. Chem.* **261–262** 123 (1998)
241. B Blumich, P Blumler, L Gasper, A Guthausen, V Gobbels, S Laukemper-Ostendorf, K Unseld, G Zimmer *Macromol. Symp.* **141** 83 (1999)
242. B Traub, S Hafber, U Wiesner, H W Spiess *Macromolecules* **31** 8585 (1998)
243. P Adriaensens, L Storme, R Carleer, D Vanderzande, J Gelan, V M Litvinov, R Marissen *Macromolecules* **33** 4836 (2000)
244. M Klinkenberg, P Blumler, B Blumich *Macromolecules* **30** 1038 (1997)

245. D Hauck, P Blumler, B Blumich *Macromol. Chem. Phys.* **198** 2729 (1997)
246. S L Dieckman, P Rizo, N Gopalsami, J P Heeschen, R E Botto *J. Am. Chem. Soc.* **114** 2717 (1992)
247. C Malveau, D Grandclaude, P Tekely, F Beaume, D Canet *Macromolecules* **34** 6274 (2001)
248. P T Callaghan *Principles of Nuclear Magnetic Resonance Microscopy* (Oxford: Clarendon Press, 1991)
249. J P Hornak *The Basics of MRI* (Internet-edition on Russian and English Languages); http://www.cis.rit.edu/htbooks/mri/
250. W Kuhn *Angew. Chem., Int. Ed. Engl.* **29** 1 (1990)
251. B Blümich *NMR Imaging of Materials* (London: Oxford University Press, 2000)
252. *Magn. Reson. Imaging. (Proceedings of the Third International Meeting on Recent Advances in MR Applications to Porous Media)* **14** (Special Issue) (7/8) (1996)
253. *Magn. Reson. Imaging. (Proceedings of the Fourth International Meeting on Recent Advances in MR Applications to Porous Media)* **16** (Special Issue) (5/6) (1998)
254. *Magn. Reson. Imaging. (Proceedings of the Fifth International Meeting on Recent Advances in MR Applications to Porous Media)* **19** (Special Issue) (3/4) (2001)
255. R Kimmich *NMR Tomography, Diffusometry, Relaxometry*. (Berlin; Heidelberg: Springer, 1997)
256. B Blümich, W Kuhn (Eds) *Magnetic Resonance Microscopy. Methods and Applications in Materials Science, Agriculture and Biomedicine* (Weinheim: VCH, 1992)
257. B Blümich P Blümler, R Botto, E Fukushima (Eds) *Spatially Resolved Magnetic Resonance. Methods, Materials, Medicine, Biology, Rheology, Geology, Ecology, Hardware* (Weinheim: Wiley-VCH, 1998)
258. B Hills *Magnetic Resonance Imaging in Food Science* (New York: Wiley, 1998)
259. W E Kenyon *Log Analyst* 21 (1997)
260. P J Prado, B Blümich, B J Balcom, in *Spectroscopy in Process Analysis* (Ed. J M Chalmers) (Sheffield: Academic Press-CRC Press, 2000) p. 234
261. R M E Valckenborg, Ph.D. Thesis, Eindhoven University of Technology, Eindhoven, 2001; http://www.phys.tue.nl/nfcmr/PhDthesis.html
262. H Van As, D van Dusschoten *Geoderma* **80** 389 (1997)
263. L Pel Ph.D. Thesis Eindhoven University of Technology, Eindhoven, 1995; http://www.phys.tue.nl/nfcmr/PhDthesis.html
264. L F Gladden *Chem. Eng. Sci.* **49** 3339 (1994)
265. L F Gladden, P Alexander *Meas. Sci. Technol.* **7** 423 (1996)
266. L F Gladden *Top. Catal.* **8** 87 (1999)
267. P Jezzard, J J Attard, T A Carpenter, L D Hall *Prog. Nucl. Magn. Reson. Spectrosc.* **23** 1 (1991)
268. J B Miller *Prog. Nucl. Magn. Reson. Spectrosc* **33** 273 (1998)
269. *Appl. Magn. Reson.* **8** (Special Issue) (3–4) (1995)
270. J A Hopkins, J B Grutzner *J. Magn. Reson., Ser. A* **111** 17 (1994)
271. R J Hayward, K J Packer, D J Tomlinson *Mol. Phys.* **23** 1083 (1972)
272. A J Lucas, S J Gibbs, E W G Jones, M Peyron, J A Derbyshire, L D Hall *J. Magn. Reson., Ser. A* **104** 273 (1993)
273. M Hallmann, K K Unger, M Appel, G Fleischer, J Karger *J. Phys. Chem.* **100** 7729 (1996)
274. A H Chung, K Hynynen, V Colucci, K Oshio, H E Cline, F A Jolesz *Magn. Reson. Med.* **36** 745 (1996)
275. R Matsumoto, R V Mulkern, S G Hushek, F A Jolesz *J.Magn. Reson. Imaging* **4** 65 (1994)

[a] — *Theor. exp. Chem. (Engl. Transl.)*